A tale of two transitions: the unfolding mechanism of the prfA RNA thermosensor

Huaqun Zhang¹, Ian Hall², Amos J. Nissley², Kyrillos Abdallah^{1,2}, Sarah C. Keane^{1,2*}

¹ Biophysics Program, University of Michigan, Ann Arbor, Michigan 48109, United States

² Department of Chemistry, University of Michigan, Ann Arbor, Michigan 48109, United States

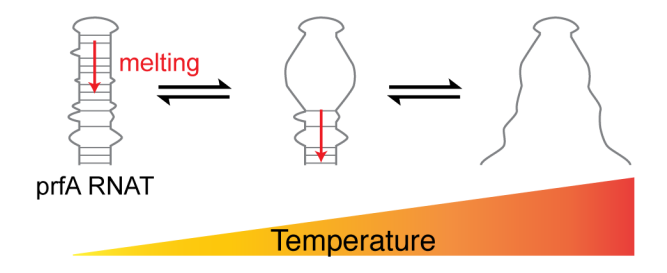
* Corresponding author: sckeane@umich.edu

RNAT structure, unfolding energetics, and translational control.

Abstract

RNAs (mRNAs), control the translation of the downstream gene in a temperature-dependent manner. In *Listeria monocytogenes*, the expression of a key transcription factor, PrfA, is mediated by an RNAT in its 5' UTR. PrfA functions as a master regulator of virulence in *L. monocytogenes*, controlling the expression of many virulence factors. The temperature-regulated expression of PrfA by its RNAT element serves as a signal of successful host invasion for the bacteria. Structurally, the prfA RNAT bears little resemblance to known families of RNATs and prior studies demonstrated that the prfA RNAT is highly responsive over a narrow temperature range. Herein we have undertaken a comprehensive mutational and thermodynamic analysis to ascertain the molecular determinants of temperature sensitivity. We provide evidence to support that the prfA RNAT unfolding is different from that of cssA, a well-characterized RNAT, suggesting that these RNATs function via distinct mechanisms. Our data show that the unfolding of the prfA RNAT occurs in two distinct events and that the internal loops play an important role in mediating the cooperativity of RNAT unfolding. We further demonstrated that regions distal to the ribosome binding site (RBS) contribute not only to RNAT structural stability, but also impact translation of the downstream message. Our collective results provide insight connecting the thermal stability of the prfA

TOC graphic



For Table of Contents use only.

Introduction

The 5' and 3' untranslated regions (UTRs) of messenger RNAs (mRNAs) can be highly structured and play a crucial role in post-transcriptional gene expression, regulating myriad events including translation, pre-mRNA processing, and viral replication. ¹⁻⁴ The 5' UTR of certain mRNAs can modulate downstream gene translation in response to changing environmental stimuli, including pH, metabolite concentration, and temperature. ⁵⁻¹⁰ Regulatory elements that respond to temperature are known as RNA thermosensors or thermometers (RNATs). To date, tens of RNATs have been identified in bacteria. ¹⁰ Most RNATs regulate gene expression by adopting a hairpin fold which harbors and sequesters the ribosome binding site (RBS) and, in some cases, also the AUG start codon at low temperatures. Release of the RBS at high temperatures allows for ribosome access and subsequent translation initiation.

Most RNATs are associated with bacterial adaptation to heat or cold stress, pathogenicity, or immune evasion. ¹⁰⁻¹² Repression of heat-shock gene expression (ROSE) elements are the most prevalent class of RNATs identified to date. In rhizobial, α- and γ-proteobacteria, ROSE elements regulate the expression of a large number of heat-shock chaperone proteins. ¹³⁻¹⁵ FourU RNATs represent a second common class of RNAT elements, so called due to the presence of four uridines that base pair with the RBS sequence. FourU RNATs have been identified in several pathogenic bacteria, including *Salmonella enterica*, ¹⁶ *Shigella dysenteriae*, ¹⁷ and *Yersinia pseudotuberculosis*, ¹⁸ where they participate in the regulation of heat shock and virulence genes. Not all RNAT elements have identifiable common sequence or structural motifs. For example, the 5' UTR of the *Neisseria meningitides cssA* gene acts as an RNAT, regulating the expression of a protein involved in capsule synthesis, but lacks sequence and structural homology to other known RNAT classes. ¹² The *Listeria monocytogenes* prfA RNAT highlights a second example of an RNAT element that does not fit into a classic RNAT family.

The prfA RNAT regulates the expression of positive regulatory factor A (PrfA), a transcription factor responsible for the expression of nine key virulence genes in *L. monocytogenes*, ¹⁹ in a temperature-dependent manner. ²⁰ Because of the central role that PrfA plays in pathogenicity of *L. monocytogenes*, it is commonly referred to as the "master regulator" of bacterial virulence. ²¹ PrfA expression levels, and

therefore the virulence of the bacterium, are controlled in a temperature-dependent manner.²⁰ At temperatures below 30 °C the expression of PrfA is extremely low, whereas at elevated temperatures (above 37 °C) PrfA is robustly expressed.²⁰ The secondary structure of the prfA RNAT was previously determined using chemical and enzymatic probing methods.²⁰

The structure and unfolding mechanism of the cssA RNAT was recently determined using a combination of chemical probing, solution NMR spectroscopy, small angle X-ray scattering, and ultraviolet melting studies.²² These studies revealed that the cssA RNAT is precisely tuned to regulate translation over a narrow physiological temperature range. Collectively, Barnwal et al. demonstrate that the cssA RNAT functions as a rheostat, where the progressive unfolding of the RNAT corresponds to an increase in translation.²²

The sequences and secondary structures of prfA and cssA RNATs are notably different and these RNATs have been used to illustrate distinct regulatory mechanisms. ¹² Both of these RNATs form stable hairpin structures at low temperature, sequestering their RBSs, ^{20, 22} yet little is known about the underlying energetics of the structural rearrangements that occur at elevated temperatures.

This study was carried out to investigate the differences in mechanism of the cssA and prfA RNATs and to understand how different regions of prfA RNAT affect the unfolding processes, energetics, and gene expression. We found that the prfA RNAT unfolds via a two-transition process and the first transition, which occurs at 37 °C, is consistent with the important role that prfA plays in regulating the virulence of *L. monocytogenes* upon invasion of a mammalian host.²³ The two internal loops surrounding the RBS and AUG regions are key structural features that induce the multiple unfolding events in the prfA RNAT. In addition to regions near the RBS sequence and AUG start codon, distal regions play a role in the stability of the RNA structure and importantly in regulating downstream gene translation. Our findings provide important insights into how the prfA RNAT, a key control mechanism for bacterial virulence, functions at a molecular level.

Methods

Cloning and construct design.

Plasmids for in vitro transcription:

The 5' UTRs of prfA (nucleotides 15-127) and cssA (nucleotides 29-99) mRNA with an upstream T7 promoter sequence and 5' hammerhead ribozyme sequence were purchased from GENEWIZ in a pUC57 plasmid. Mutations and/or deletions were introduced via site-directed mutagenesis using the Q5 site-directed Mutagenesis Kit (New England Biolabs) using primers listed in **Table S1**. All primers were purchased from Integrated DNA Technologies. Plasmids were verified by Sanger sequencing (University of Michigan Sequencing Core) using the universal M13REV sequencing primer.

Plasmids for cell-based expression:

pBS SK(+)-prfA-GFP was constructed based on a previous study.²⁴ Briefly, a gene block, containing the tobacco plastid rRNA operon promoter *Prrn*, the *prfA* 5' UTR including four amino acids of the downstream coding sequence, the GFP coding region, and the 3' UTR of the plastid *rps16* gene, was ordered from GenScript. To facilitate restriction-digestion cloning, *Sac I* and *Hind III* restriction sites were included at the 5' and 3' end of the gene block, respectively. The cloning vector pBlueScript II SK (+) [pBS SK(+)] was purchased from Agilent Technologies. The gene block was amplified using primers PBS-prfA_Fwd and PBS-prfA_Rev (Table S1), and then purified with the Genejet PCR purification kit (Thermo Fisher Scientific). The purified gene and pBS SK(+) vector were digested by restriction enzymes *Sac I* and *Hind III*, followed by ligation using the Quick T4 Ligation Kit (New England Biolabs). Ligation product was transformed into DH5α competent cells (Invitrogen). Plasmids were then isolated from overnight cell cultures in liquid broth supplemented with 100 μg/mL ampicillin (Amp⁺). As described above, mutations and/or deletions were introduced via site-directed mutagenesis with the Q5 site-directed Mutagenesis Kit (New England Biolabs) using primers listed in Table S1. Plasmids were verified by Sanger sequencing (University of Michigan Sequencing Core) using universal T7 and M13REV sequencing primers.

RNA preparation.

DNA templates for *in vitro* transcription were PCR-amplified from the appropriate plasmids using primers PUC57-80-Fwd and HH-prfA-Rev (**Table S1**) with EconoTaq PLUS 2x Master Mix (Lucigen). RNAs were prepared by *in vitro* transcription in 1X transcription buffer (40 mM Tris-base, 5 mM DTT, 1 mM Spermidine, 0.01% Triton-X, pH 8.5) with addition of 3-6 mM NTPs, 10-20 mM MgCl₂, 30-40 ng/uL DNA template, 0.2 U/mL yeast inorganic pyrophosphatase (New England Biolabs),²⁵ ~15 μM T7 RNA polymerase, and 10-20% (vol/vol) DMSO.²⁶ Reactions were incubated at 37 °C for 3-4 hours and then quenched using a solution of 7M urea and 250 mM EDTA (pH 8.5). The transcription mixture was loaded onto 10% preparative-scale denaturing gels for RNA purification. Gel slices containing target RNA were crushed and then soaked in TBE buffer. RNAs were spin concentrated, salt washed and water exchanged using Amicon Centrifugal Filter Units (Millipore, Sigma). RNA purity was checked by running RNA on a 10% analytical denaturing gel. RNAs were refolded by heating in boiling water for 3 min in H₂O, followed by incubation on ice for 3 min, and then RNAs were transferred to lyophilized buffer for subsequent experiments. Sequences for all RNA constructs are given in **Table S2**.

Preparation of phosphate buffer.

50 mM $K_xH_yPO_4$ pH = 6.5 was prepared by dissolving 0.033 moles of KH_2PO_4 and 0.017 moles of K_2HPO_4 in 1 L of water. The total K^+ concentration is 67 mM.

Native gel electrophoresis.

15 μ M RNA was prepared in 50 mM K_xH_yPO₄ pH = 6.5 buffer and incubated at 4 °C for 30 minutes. 50% glycerol, pre-incubated at 4 °C, was added to each RNA sample (20% vol/vol). The samples were immediately mixed and loaded onto a 10% native polyacrylamide gel. Gels were run at 30 V, 4 °C and the buffer was mixed thoroughly every 15 minutes. The native gel and running buffer were prepared to a final 1x buffer: 50 mM Hepes, 50 mM KCl, pH = 7.6 to better preserve the RNA conformation.²⁷

NMR spectroscopy.

NMR spectra were collected on a 800 MHz Bruker Avance Neo spectrometer equipped with a 5mm TCI cryogenic probe (University of Michigan BioNMR Core) or a 750 MHz Bruker Avance III HD spectrometer equipped with a 5mm TXI cryogenic probe (University of Wisconsin-Madison NMRFAM). RNA samples were prepared in 50 mM K_xH_yPO₄ pH = 6.5 buffer. 1D imino proton spectra were recorded at 20 °C using buffers that contained 10% D₂O. Aromatic 1D proton and 2D ¹H-¹H NOESY spectra were recorded in 100% D₂O. 1D NMR data were processed and analyzed with MestreNova 12.0.4 (Mestrelab Research SL, Santiago de Compostela, Spain). 2D NMR data were processed with NMRFx and analyzed with NMRViewJ.^{28, 29} Aromatic proton assignments were made based on comparison with small RNA controls.

Circular dichroism spectroscopy.

Circular dichroism (CD) experiments for all RNA constructs were carried out on a JASCO J-1500 spectropolarimeter (JASCO) equipped with a temperature control module. RNA unfolding and folding experiments were performed at 260 nm from 5 °C to 95 °C and back to 5 °C with a heating or cooling rate of 1 °C/min. The bandwidth was set to 5 nm, CD and FL scales were 200 mdeg/1.0 dOD with a digital integration time of 1 sec. Both CD and total absorbance at 260 nm were monitored. 15 μ M RNA sample in 50 mM K_xH_yPO₄ (pH = 6.5) was used for CD measurements (unless otherwise indicated) in a cuvette with a sample length of 1 mm. The RNA concentration was determined via UV absorbance before each experiment. The derivative of the absorbance at 260 nm was obtained using a finite difference method. Normalized CD data and the derivative of absorbance were smoothed using a five-point moving average in Matlab. Thermodynamic parameters were extracted by fitting first derivatives of the absorbance data with a one- or two-transition model in Prism (see supplement for fitting models). The entropy change of each transition, Δ S_n, was determined by eq 1.

$$\Delta S_n = \frac{\Delta H_n}{T_{m,n}} \qquad (1)$$

Calculation of the standard free energy change for each transition, ΔG°_{n} , was calculated at 25 °C using ΔH_{n} and ΔS_{n} .

Differential scanning calorimetry.

Differential scanning calorimetry (DSC) experiments were conducted on a Nano DSC instrument (TA Instruments). Samples were prepared as described above with an RNA concentration of \sim 60 μ M in 50 mM $K_xH_yPO_4$ pH = 6.5 buffer. The same phosphate buffer was used as the reference solution. Samples were degassed under vacuum for 5 min and then loaded onto the calorimeter. Before each experiment, the RNA concentration was determined via UV absorbance. During each experiment samples were pressurized to 3 atm and then heated from 5 °C to 95 °C at a rate of 1 °C/min. The DSC data were analyzed with NanoAnalyze software (TA Instruments). The raw data were converted to molar heat capacity and fit with two two-state scaled models (see supplement for fitting model). Enthalpy values for each transition, ΔH_n , were derived from the area under the fitted curves. The entropy change of each transition, ΔS_n , was determined by eq 1. Calculation of the standard free energy change for each transition, ΔG°_n , was calculated at 25 °C using ΔH_n and ΔS_n .

GFP reporter assay.

Plasmids encoding prfA-GFP constructs were transformed into DH5 α cells (Invitrogen) and plated on Amp⁺ LB agar. Plates were incubated at 30 °C overnight followed by inoculation to 3 mL Amp⁺ LB medium and cultured overnight at 30 °C. Untransformed DH5 α cells were used as negative control. The following day, the OD₆₀₀ of all cell cultures was measured and overnight cultures were used to inoculate a fresh 3 mL Amp⁺ LB to a starting OD₆₀₀ of 0.04. Cultures were incubated with shaking at 37 °C until the OD₆₀₀ reached ~0.6. Cultures were pelleted (16,873 x g, 1min), the liquid media was decanted, and the cell pellets washed once with 200 μ L of wash buffer (50 mM Tris-base, 150 mM NaCl, pH 7.5). Cells were resuspended with 200 μ L wash buffer and diluted to OD₆₀₀ = 1.2. 150 μ L of sample was transferred to a 96-well BioLite microwell plate (Thermo Fisher Scientific) in triplicate and GFP fluorescence was

measured using a POLARstar Omega Plate Reader (BMG LABTECH) with excitation wavelength at 485 nm and emission at 520 nm. Assays were repeated at least 3 times.

Results

The prfA and cssA RNATs have distinct unfolding mechanisms.

Prior work shows that the cssA RNAT functions as a rheostat, gradually increasing GFP expression as temperature increases.²² In contrast, the prfA RNAT appears to have a distinct mechanism of translational control, robustly expressing a GFP reporter only when the temperature increased above 37 °C. 12 These observations lead to the hypothesis that the prfA thermosensor acts as a molecular 'switch' for turning on downstream gene translation. 12 The similarities and differences between the translational control of the prfA and cssA RNATs and the energetic parameters that govern their unfolding mechanisms remain unknown. Therefore, we conducted thermal melting experiments on both the prfA and cssA RNATs using CD spectroscopy (Fig. 1a-c). The thermal denaturation of the cssA RNAT appears to have a single sharp unfolding transition, (Fig. 1c), consistent with previous studies.²² In contrast, the prfA RNAT thermal denaturation under the same conditions has a much broader unfolding profile as observed by CD spectroscopy with two distinct thermal transitions at 37.2 °C and 44 °C (Fig. 1c, Fig. S1, and Table S3). Both cssA and prfA RNATs have reversible unfolding pathways (Fig. S2), which are consistent with the need for the bacteria to regulate gene expression under constantly changing environmental temperatures. The melting temperatures and thermodynamics parameters derived from analysis of the CD data (see Supplemental Materials) are presented in Table S3. To directly measure the energetics of these transitions, we performed DSC on both cssA and prfA RNATs. Consistent with the CD-based thermal denaturation experiments, our DSC studies revealed that cssA unfolds in a highly cooperative manner, with a single predominant unfolding transition at 36.2 °C which largely overlaps a minor transition at 40 °C (Fig. 1d, Fig. S3 and Table 1). In contrast, the prfA RNAT has two overlapping, but visibly distinct transitions at 37.0 °C and 46.4 °C (Fig. 1e and Table 1). Raw DSC traces for cssA and prfA, prior to baseline subtraction and analysis, are shown in Figure S4. In both the cssA and prfA

RNAT unfolding studies, we observe a minor third transition at high temperatures that we attribute to either misfolded RNA or RNA aggregates.²² Native gel electrophoresis of the cssA and prfA RNATs reveals that these RNAs are largely homogeneous in conformation, with small amounts of aggregation detected (**Fig. S5**). Both RNATs possess enthalpically-driven, endergonic free energies of unfolding (**Table 1**). However, the cssA RNAT has a lower free energy of unfolding relative to the prfA RNAT counterpart indicating that the prfA RNAT has a more stable overall structure.

Our dual CD and DSC experimental approach revealed some notable differences in thermodynamic parameters obtained using each method. Monitoring thermal unfolding by both CD spectroscopy and DSC provides additional insight into the thermodynamics of RNA melting. While DSC measures the total energy associated with RNA melting (including loops and non-canonical structures), CD spectroscopy (at 260 nm) predominately reports the energy associated with unfolding of A-helical structures. Thus, the combination of techniques allows one to differentiate the energy associated with unfolding of A-helical elements from other structures. As such, all comparison of melting temperatures and thermodynamic parameters will be based on our DSC data (**Table 1**).

Finally, analysis of the peak width (full-width half-max, FWHM) derived from fits of the DSC data for the prfA RNAT suggest reduced cooperativity relative to unfolding of the cssA RNAT (**Table S4**).^{32, 33} Collectively, these data confirm that the prfA RNAT unfolds via a distinct mechanism relative to the cssA RNAT and warrants further investigation of the sequence and structural determinants of temperature sensitivity.

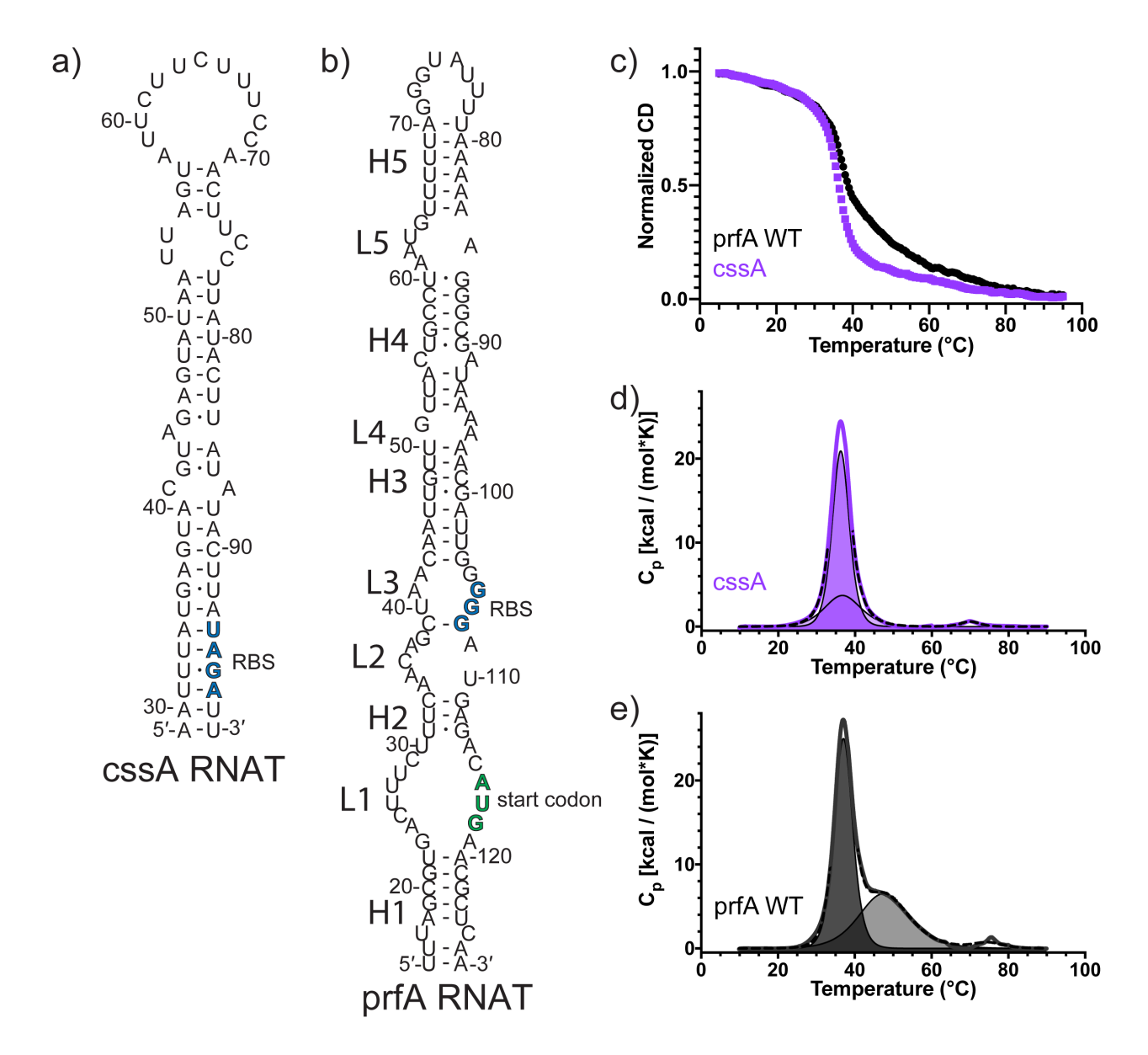


Figure 1. The cssA and prfA RNATs have unique unfolding properties. Secondary structures of the cssA²² (a) and prfA²⁰ (b) RNATs. The RBS and AUG codon (prfA only) are highlighted in blue and green, respectively. (c) Overlay of CD melting curves of cssA (purple) and prfA (black) RNATs monitored at 260 nm. DSC unfolding curves of cssA RNAT (d) and prfA RNAT (e). Processed DSC data is plotted as a solid colored line, a fit for each individual transition is shown as a solid black line with shading underneath, and the dashed line indicates the sum of the fitted curves in both (d) and (e).

Table 1. Thermodynamic parameters for RNAT unfolding derived from DSC data.

Construct	T_{ml}	ΔH_1	ΔS_1	ΔG°_{1}	T_{m2}	ΔH_2	ΔS_2	ΔG°_{2}	ΔG°_{total}	$\Delta\Delta G^{\circ}_{total}$
	(°C) ^a	(kcal/mol)a	[cal/(mol•K)]	(kcal/mol)a,b	(°C) ^a	(kcal/mol)a	[cal/(mol•K)]	(kcal/mol)a,	(kcal/mo	(kcal/mol)
			a				a	b	1) ^c	WT-mut ^d
cssA	36.2 ± 0.4	130 ± 10	410 ± 30	4.6 ± 0.2	40 ± 2	20 ± 10	80 ± 40	1.1 ± 0.4	5.7 ± 0.4	-
prfA-WT	37.0 ± 0.6	149 ± 5	480 ± 20	5.9 ± 0.1	46.4 ± 0.8	114.9 ± 0.6	360 ± 2	7.8 ± 0.3	$13.7 \pm$	0
									0.3	
prfA-U46A	32.71 ± 0.05	107 ± 4	350 ± 10	2.74 ± 0.09	46.7 ± 0.2	83 ± 4	260 ± 10	5.7 ± 0.3	8.4 ± 0.3	5.3 ± 0.4
prfA-3C	43.4 ± 0.5	90 ± 10	290 ± 30	5.4 ± 0.7	57.8 ± 0.1	170 ± 20	500 ± 60	17 ± 2	22 ± 2	-9 ± 2
prfA-L1 _{stab}	46.4 ± 0.2	160 ± 20	490 ± 60	11 ± 1	49 ± 1	60 ± 20	180 ± 50	4 ± 1	15 ± 1	-1 ± 1
prfA-L2 _{stab}	45.6 ± 0.3	220 ± 20	680 ± 60	14 ± 1	48 ± 1	80 ± 30	260 ± 80	6 ± 2	20 ± 2	-6 ± 2
prfA-L5 _{stab} e	40.52 ± 0.02	184 ± 9	590 ± 30	9.2 ± 0.4	50.94 ± 0.05	150 ± 10	450 ± 40	12 ± 1	21 ± 1	-8 ± 1
prfA-C58G	31.62 ± 0.09	164 ± 4	540 ± 10	3.63 ± 0.04	45.4 ± 0.1	126 ± 7	400 ± 20	8.1 ± 0.4	11.7 ± 0.4	2.0 ± 0.5
prfA-H4 _{destab}	32.22 ± 0.06	161 ± 6	530 ± 20	3.9 ± 0.2	42.7 ± 0.3	120 ± 20	370 ± 50	7 ± 1	11 ± 1	3 ± 1

 $^{^{}a}V$ alues of ΔH , ΔS , ΔG° , and T_{m} , are represented as the average of three replicate measurements \pm the standard deviation.

^bAt 25 °C.

 $^{^{}c}\Delta G^{\circ}_{total}$ is the sum of ΔG°_{1} and ΔG°_{2} . Error was propagated from the errors associated with ΔG°_{1} and ΔG°_{2} .

 $^{^{}d}\Delta\Delta G^{\circ}_{total}$ is defined as $\Delta G^{\circ}_{total\text{-}WT}$ - $\Delta G^{\circ}_{total\text{-}mutant}.$ Error was propagated from the errors associated with $\Delta G^{\circ}_{total\text{-}WT}$ and $\Delta G^{\circ}_{total\text{-}mutant}.$

^eprfA L5_{stab} values are based on two replicate measurements.

Effect of Mg^{2+} and K^{+} concentration on the unfolding of prfA and cssA RNATs.

Metal ions are known to play important roles in the structure, function, and structural stability of various RNA molecules. $^{34-36}$ Therefore, we investigated the importance of both mono- and di-valent cations on the unfolding of the prfA RNAT. CD thermal denaturation experiments were carried out in a sodium phosphate buffer (50 mM Na_xH_yPO₄, pH = 6.5) rather than potassium phosphate, as described above. Under these conditions, the prfA RNAT exhibits a nearly identical two-transition melting profile (**Fig. S6a**). While the identity of the monovalent ion does not appear to alter the structural stability and unfolding profile of the prfA RNAT, we next examined how the concentration of K⁺ affected the stability of the RNAT structure. To test if the structural stability of the prfA RNAT is driven by the concentration of monovalent ions, we measured the unfolding profile of the prfA RNAT in buffers containing increasing concentrations of K⁺ from 67 mM to 192 mM. We found that increasing K⁺ concentration does not change the unfolding profile of the prfA RNAT, but stabilizes the RNAT as a whole, shifting both melting temperatures (**Fig. S6b, Table S5**). This is consistent with previous findings that monovalent ions stabilize RNA duplex structures. 37,38 Analysis of the ion-dependence data (**Fig. S6c**) revealed that ~5 K⁺ ions are released in the first unfolding event while ~1 K⁺ ion is released in the second.

We then tested the role of divalent cations in prfA RNAT folding. We added 1 μ M EDTA to the 50 mM K_xH_yPO₄ buffer (pH = 6.5) to chelate trace divalent ions. Addition of 1 μ M EDTA resulted in an unchanged folding profile relative to the EDTA-free buffer (**Fig. S6d**). Because EDTA has been shown to be a weak chelator of Mg²⁺ in low pH buffers,³⁹ we also examined the effect of adding higher concentrations of EDTA to the samples. We found that addition of mM concentrations of EDTA did not destabilize the RNATs, but rather slightly stabilized them, presumably due to the increased total monovalent ion concentration due to the addition of Na₂-EDTA (**Fig. S6e**). Subsequently, using the 50 mM K_xH_yPO₄ buffer (pH = 6.5) with 1 μ M EDTA, we titrated Mg²⁺ to a final concentration of 5 mM (**Fig. S6d**). Increasing Mg²⁺ concentration stabilizes the prfA RNAT to a greater extent than increasing K⁺ concentration, consistent with previous studies that show Mg²⁺ has a stronger stabilizing effect than K^{+.40}.

⁴¹ We found the same trends for both mono- and di-valent ions hold true for the cssA RNAT under these same experimental conditions (**Fig. S7**).

U46A and 3C mutations affect the prfA RNAT unfolding thermodynamics.

Prior studies of the prfA RNAT using both in vitro and cell-based gene expression assays, demonstrated that a single point mutation, U46A (Fig. 2a), led to robust expression of the downstream gene at a low temperature (30 °C).²⁰ Conversely, a triple mutant, U40C-A41C-A42C (3C, Fig. 2b), dramatically reduced downstream gene expression even at elevated temperatures.²⁰ Nevertheless, it is not clear how those mutations affect the energetics of prfA RNAT unfolding. Therefore, we carried out CD and DSC thermal denaturation experiments on prfA-U46A and -3C RNAT constructs. Our CD data show that the U46A mutant is destabilized and the 3C mutant is stabilized relative to the WT RNAT (Fig. 2c and Table S3). Consistent with our observations of the WT prfA RNAT, both the U46A and 3C mutants are characterized by two unfolding events (Fig. 2d,e). The first unfolding event in U46A is shifted -4.3 °C relative to WT while the 2^{nd} unfolding transition remains unchanged (**Table 1**). The ΔG°_{total} for the prfA-U46A RNAT is 8.4 kcal/mol, 5.3 kcal/mol destabilized relative to the prfA-WT RNAT (**Table 1**). Overall, the U46A mutation slightly increases the total peak width, indicating a reduction of the cooperativity of RNAT unfolding (Table S4). For the prfA-3C RNAT, both transitions appear to be stabilized. An additional striking feature of the prfA-3C RNAT is that the second transition, rather than the first, appears to be the major unfolding event (Fig. 2e). One alternative interpretation of these results is that the 3C mutation dramatically stabilizes the main unfolding (T_{m2} in prfA-3C increases by ~ 20 °C relative to T_{m1} in prfA-WT, Table 1) while the minor unfolding transition is slightly destabilized relative to WT (T_{ml} in prfA-3C decreases by 3 °C relative to T_{m2} in prfA-WT, **Table 1**). The 3C mutation results in formation of three additional GC base pairs to close the L3 loop, effectively extending helix H3. Therefore, the latter interpretation appears to fit our data best. The structural stabilization afforded by the 3C mutations leads to a highly cooperative unfolding of the top of the RNAT in its main transition (**Table S4**).

The 3C-stabilized RNAT does not activate translation at 37 °C, as is characteristic of the prfA-WT RNAT, 20 consistent with our findings that the main unfolding event of the prfA-3C RNAT occurs at significantly higher temperatures (~57 °C). The prfA-3C RNAT has a ΔG°_{total} of 22 kcal/mol, which is stabilized relative to WT ($\Delta\Delta G^{\circ}_{total}$ = -9 kcal/mol, **Table 1**). As with the prfA-WT RNAT the transitions of the U46A and 3C mutants are enthalpically driven (**Table 1**). The underlying energetics of RNAT unfolding in these two constructs provides a plausible explanation for the modulation of temperature-dependent gene expression observed in previous studies. 20

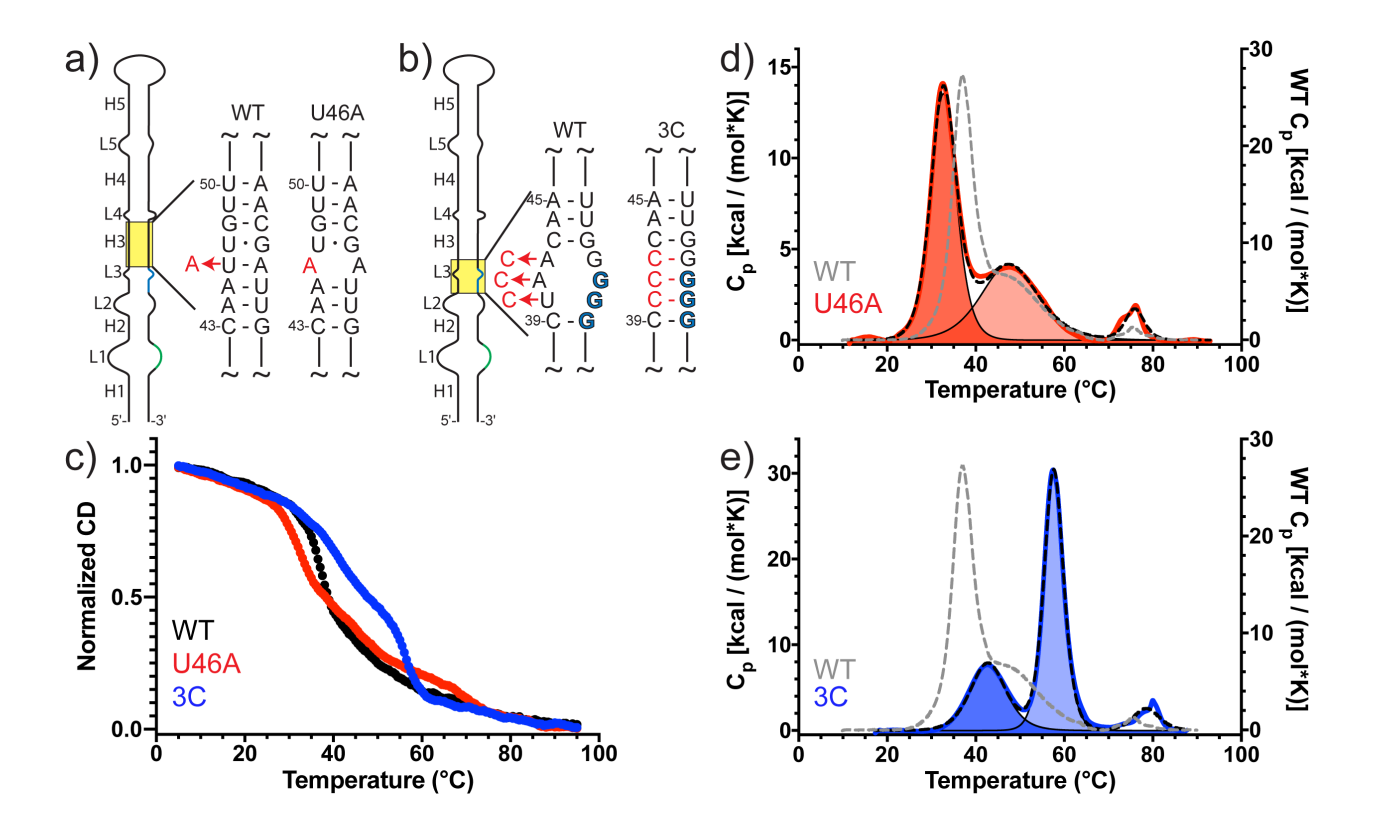


Figure 2. Thermal melting of prfA-U46A and -3C RNATs. Schematic representation of the prfA-U46A (a) and prfA-3C (b) RNAT constructs with mutations indicated (left) and the resulting predicted secondary structures (right). (c) Overlay of CD melting curves of prfA-WT (black), -U46A (red) and -3C (blue) RNATs monitored at 260 nm. DSC unfolding curves of prfA-U46A (d) and -3C RNATs (e). Processed DSC data is plotted as a solid colored line, a fit for each individual transition is shown as a

solid black line with shading underneath, and the dashed line indicates the sum of the fitted curves in both (d) and (e). The processed prfA-WT RNAT DSC data are shown as a grey dashed line for comparison in (d) and (e).

Folding cooperativity of prfA RNAT is enhanced by reducing the size of its internal loops.

Mutations to the H3 and L3 regions (U46A and 3C, respectively) have pronounced differences in the regulation of translation by the prfA RNAT.²⁰ Our data suggest that the changes in the regulation are governed by changes in the underlying energetics that affect the structural stability of regions proximal to the RBS. To understand how stabilization of other loop regions affects the unfolding of the prfA RNAT we generated stabilization mutants in the L1 and L2 regions: L1_{stab} and L2_{stab}, respectively (Fig. 3a,b). Next, we carried out thermal denaturation assays, monitored by both CD spectroscopy and DSC. Both L1_{stab} and L2_{stab} constructs display a shift toward a higher melting temperature and have a sharper inflection in the CD melting curve, reminiscent of a single two-state unfolding transition (Fig. 3c). The effect of both L1_{stab} and L2_{stab} mutations is perhaps most striking when monitored by DSC. The prfA-WT RNAT has a distinct, bimodal unfolding curve, while both the L1_{stab} and L2_{stab} mutations are characterized by a predominant single transition overlapping a minor secondary transition (Fig. 3d,e and Fig. S3). The prfA-L1_{stab} RNAT has approximately the same stability as WT ($\Delta\Delta G^{\circ}_{total} = -1$ kcal/mol, **Table 1**) whereas the -L2_{stab} RNAT is stabilized relative to WT ($\Delta\Delta G^{\circ}_{total} = -6 \text{ kcal/mol}$, Table 1). As monitored by DSC, the stabilization afforded by the L2_{stab} substitution ($\Delta G^{\circ}_{1} = 14 \text{ kcal/mol}$, **Table 1**) is comparable to that afforded by the 3C mutations ($\Delta G^{\circ}_{2} = 17$ kcal/mol, **Table 1**), as both constructs eliminate small internal loops. L1_{stab} and L2_{stab} have reduced peak widths (FWHM) relative to WT (**Table S4**), indicative of increased cooperativity of unfolding. Analysis of the CD data with these two overlapping two-state transitions in mind revealed that these data are also best fit to a two-transition unfolding model (Table S3).

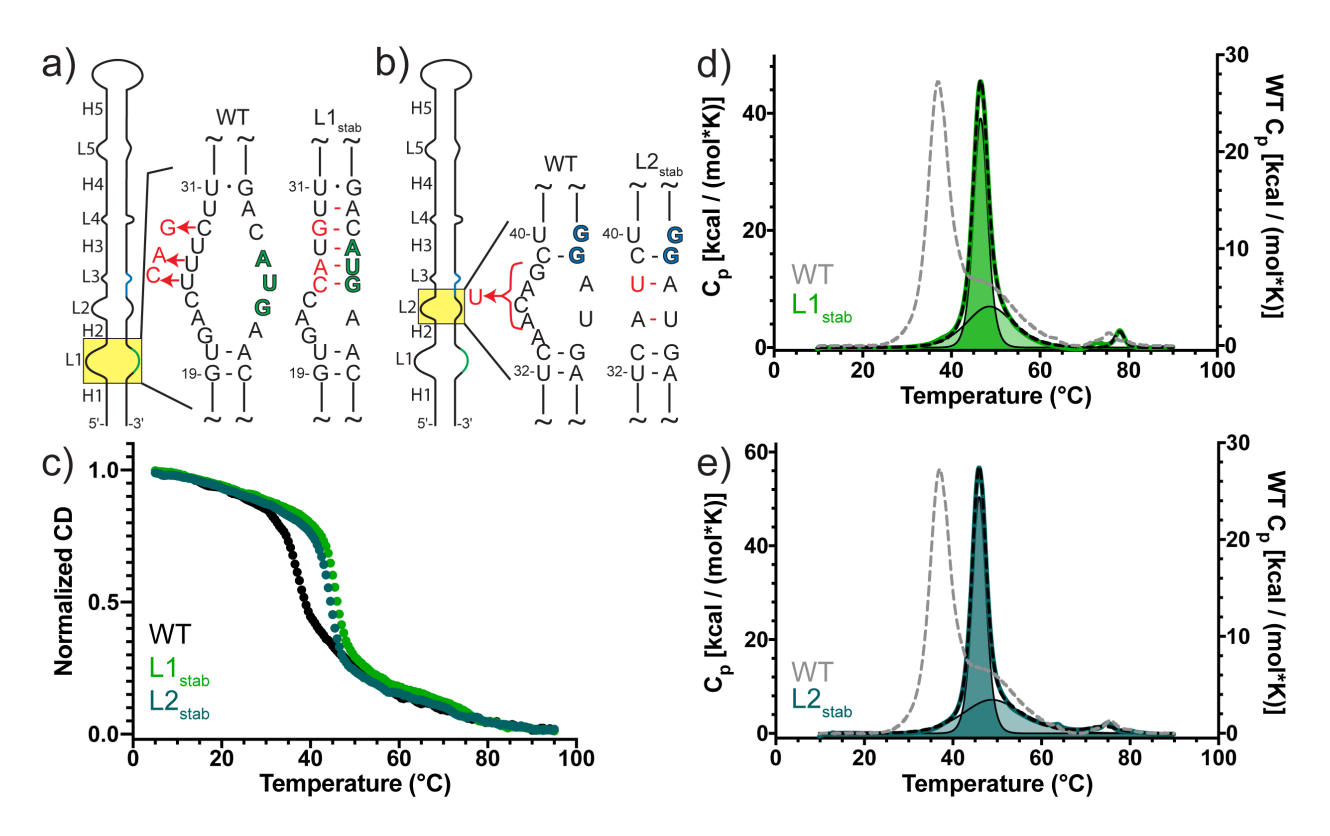


Figure 3. Unfolding mechanism is altered upon stabilization of L1 or L2 in the prfA RNAT.

Schematic representation of the construction of prfA-L1_{stab} (a) and prfA-L2_{stab} (b) RNAT constructs with mutations and/or deletions indicated (left) and the resulting predicted secondary structures (right). (c) Overlay of CD melting curves of prfA-WT (black), -L1_{stab} (green) and -L2_{stab} (teal) RNATs monitored at 260 nm. DSC unfolding curves of prfA-L1_{stab} (d) and -L2_{stab} RNATs (e). Processed DSC data is plotted as a solid colored line, a fit for each individual transition is shown as a solid black line with shading underneath, and the dashed line indicates the sum of the fitted curves in both (d) and (e). The processed prfA-WT RNAT DSC data are shown as a grey dashed line for comparison in (d) and (e).

Regions distal to the RBS affect the structural stability of prfA RNAT

We next examined the effect of mutations to the RNAT that are distal to both the RBS and the start codon. We generated a construct that stabilizes loop 5 (L5_{stab}) by removing nucleotides within L5 and generating a U-A base pair, effectively connecting H4 and H5 (**Fig. 4a**). This mutation stabilized the RNAT, as evidenced by the right shift in the CD melt (**Fig. 4b** and **Table S3**). Further analysis by DSC

(**Fig. 4c**) revealed a distinct two-transition unfolding, with an observed increase in both T_{m1} and T_{m2} (3.5 °C and 4.4 °C, respectively, **Table 1**). The prfA-L5_{stab} RNAT has an enhanced second unfolding event relative to the prfA-WT RNAT (**Fig. 4c**). This observation is in stark contrast to other stabilizing mutations, including the L1_{stab} and L2_{stab} mutations, which minimize the second unfolding event.

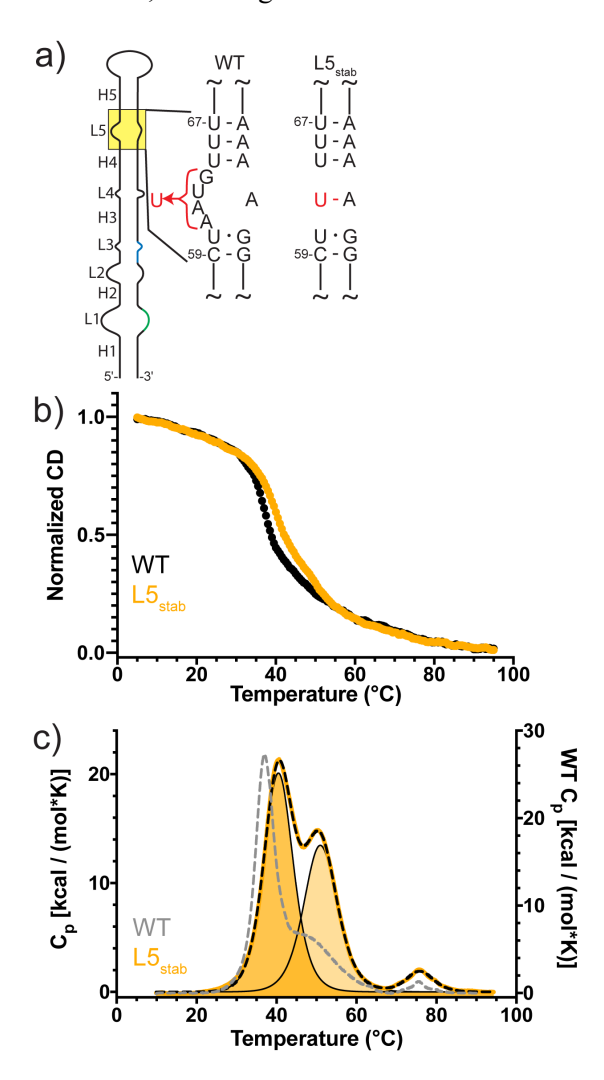


Figure 4. Thermal melting of prfA-L5_{stab} **RNAT.** (a) Schematic representation of the construction of prfA-L5_{stab} with deletions and substitution indicated (left) and the resulting predicted secondary structure (right). (b) Overlay of CD melting curves of prfA-WT (black) and -L5_{stab} (gold) RNATs monitored at 260 nm. (c) DSC unfolding curve of prfA-L5_{stab}. Processed DSC data is plotted as a solid colored line, a fit for each individual transition is shown as a solid black line with shading underneath, and the dashed line

indicates the sum of the fitted curves. The processed prfA-WT RNAT DSC data are shown as a grey dashed line for comparison in (c).

To determine the effect of destabilizing mutations in these distal regions, we characterized the RNAT structural stability and unfolding profile of two constructs which destabilize the H4 region; a single point mutation, C58G (**Fig. 5a**), and a more extensive mutant, H4_{destab} (**Fig. 5b**). The thermal melts of both the prfA-C58G and H4_{destab} constructs revealed a reduction in both T_{m1} and T_{m2} (**Fig. 5c** and **Tables 1, S3**). Surprisingly, both the prfA-C58G and -H4_{destab} RNATs have similar energetics, as monitored by DSC (**Fig. 5d,e** and **Table 1**), even though the H4_{destab} mutations are predicted to disrupt a more extensive region of secondary structure in H4, effectively expanding L5. The prfA-C58G and -H4_{destab} RNATs are destabilized relative to -WT to a similar extent ($\Delta\Delta G^{\circ}_{total} = 2$ kcal/mol and 3 kcal/mol, respectively, **Table 1**), however, the -H4_{destab} construct unfolds over a wider temperature range, indicating reduced cooperativity in the unfolding of RNAT (**Table S4**). Taken together, these results indicate that mutations to regions distal to the RBS have a comparable effect on overall stability of the RNA structure, in both magnitude and direction, to mutations near the RBS. However, these data do not inform on the extent to which regions distal to the RBS may affect translation in a temperature-dependent manner.

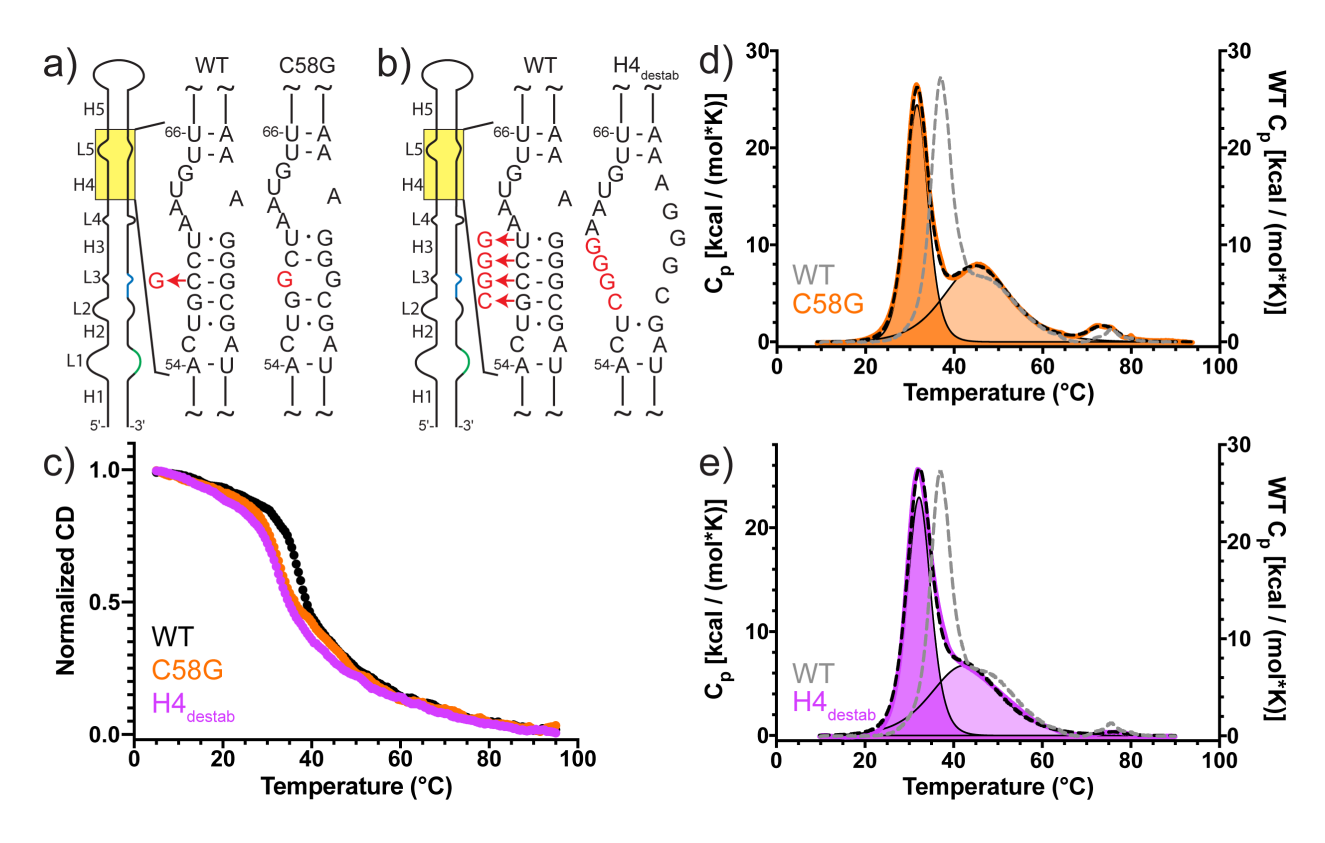


Figure 5. Thermal melting of prfA RNAT mutants that destabilize helix 4. Schematic representation of the construction of prfA-C58G (a) and -H4_{destab} (b) with site of the mutation indicated (left) and the resulting predicted secondary structure (right). (c) Overlay of CD melting curves of prfA-WT (black), - C58G (orange), and -H4_{destab} (magenta) RNATs monitored at 260 nm. DSC unfolding curve of prfA-C58G (d) and -H4_{destab} (e). Processed DSC data is plotted as a solid colored line, a fit for each individual transition is shown as a solid black line with shading underneath, and the dashed line indicates the sum of the fitted curves in both (d) and (e). The processed prfA-WT RNAT DSC data are shown as a grey dashed line for comparison in (d) and (e).

Insight into the prfA RNAT unfolding mechanism by NMR spectroscopy.

NMR spectroscopy is a powerful tool for the elucidation of structural perturbations induced by changing temperature. Chemical shift is an indicator of electronic environment, and for RNAs, can inform on base pairing. Canonical base pairs with the arrangement 'YUR:YAR' (Y, pyrimidine; R, purines; U, uridine; and A, adenosine) result in a significantly upfield shifted (between 6.5-6.7 ppm) adenosine H2

signal. 42, 43 This signature chemical shift allows for the identification of particular base pairings, even in very large RNAs. 44-49 In the prfA RNAT, these unique sets of base pairs are naturally present in the H3, H4, and H5 helices (Fig. 6a). We have unambiguously assigned the chemical shifts for adenosines A44.H2, A70.H2, A80.H2, and A93.H2, which are resolved in both 1D and 2D proton-detected experiments (Fig. 6b). Analysis of a series of temperature-dependent 1D ¹H NMR spectra reveal chemical shift changes and signal broadening, indicating significant structural changes in the prfA RNAT when the temperature is increased (Fig. 6b). Signals corresponding to A70.H2 and A80.H2 (located within H5), are noticeably downfield-shifted over the 30-35 °C range, indicating a change from paired to unpaired. Similarly, the signal corresponding to A92.H2 (within H4) experiences a downfield shift over the same temperature range. Interestingly, the A44.H2 signal, which reports on base pairing within H3, has no discernable chemical shift change over the temperature range studied, rather this signal begins to experience line broadening around 37 °C. These data, taken together with our mutational and thermodynamic analysis are consistent with the upper helical regions of the prfA RNAT (H3, H4, and H5) melting in the first unfolding transition. Unfortunately, we cannot perform the same analysis for the lower helical regions (H1 and H2) as there are no resolvable signals for these regions. Mutations which would yield a resolved signal are likely to perturb the stability of these regions and were not pursued.

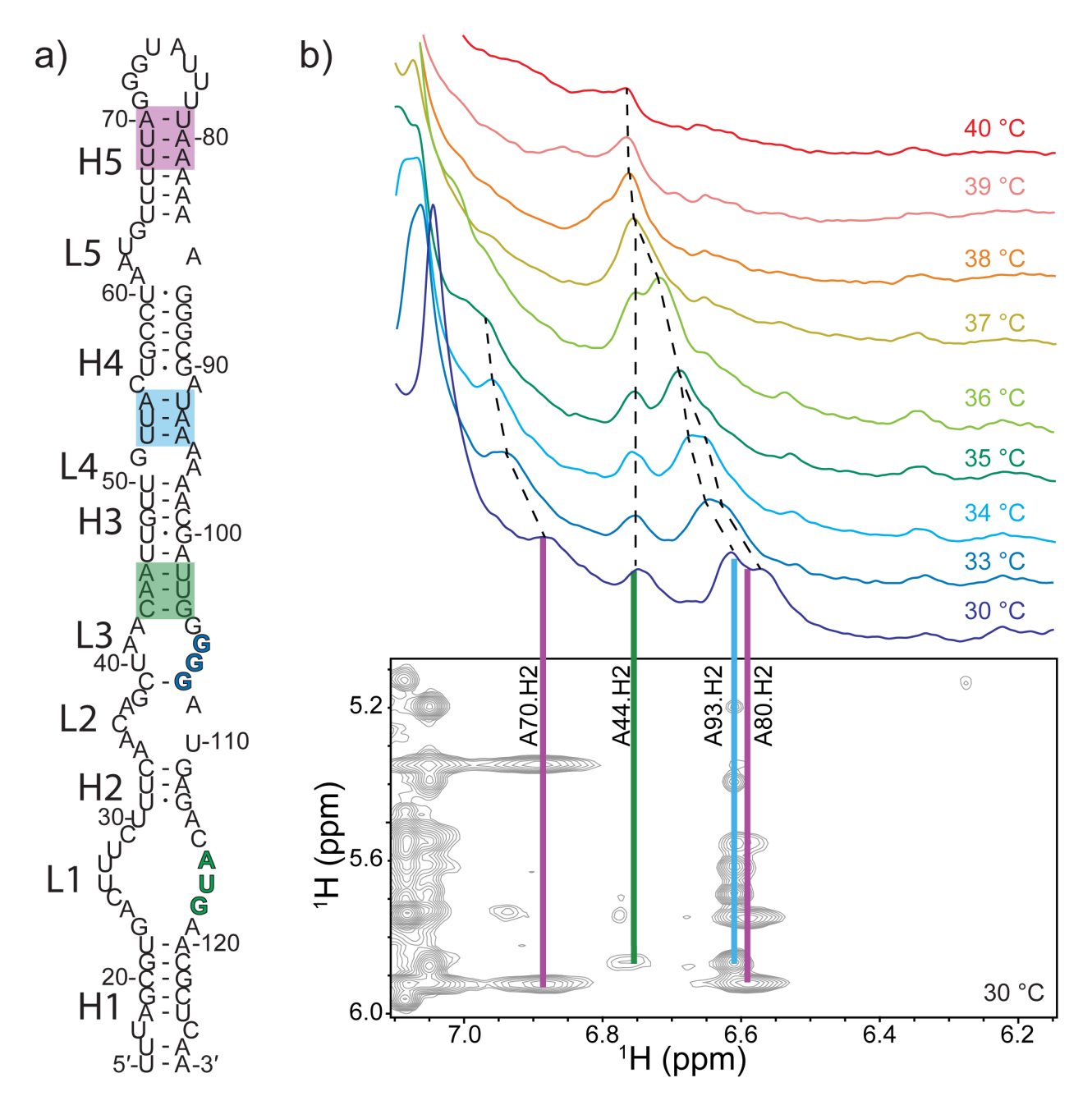


Figure 6. NMR-based analysis of prfA RNAT unfolding. (a) Secondary structure of the prfA RNAT with colored boxes indicating the three regions with distinct base pairing patterns that yield resolved proton signals. (b) NMR analysis of the prfA RNAT. 2D ¹H-¹H NOESY spectrum of the prfA RNAT (bottom) was used to assign resolved adenosine H2 signals at 30 °C. Spin systems are connected with a vertical line (colored as in (a)) and the assignments noted. These four signals are reasonably well-resolved in the 1D proton spectrum (top). A series of 1D proton spectra, collected at increasing temperature, reveal

significant spectral changes, denoted with black dashed lines. The downfield shift and/or line broadening of the identified signals is consistent with destabilization of the base pairing of these groups (highlighted in (a)).

Effect of mutation to the prfA RNAT on downstream protein expression.

We have characterized the unfolding processes of wild type prfA RNAT and its variants by monitoring secondary structure changes using CD spectroscopy and extracting the underlying energetics via DSC. Yet, it is unknown how those stabilizing and destabilizing mutations influence the translational control of the RNAT. Using a GFP reporter assay, we compared relative GFP expression under the control of prfA RNAT and prfA derivatives by measuring GFP fluorescence in E. coli cultures (Fig. 7a). As a positive control, we generated a construct (prfA- Δ 1-75) in which the first 75 nucleotides of the prfA RNAT sequence were removed, preventing the RNAT element from forming a stable secondary structure and thereby maximizing gene translation. GFP expression, when controlled by the WT prfA RNAT, was reduced to 29% of the positive control, indicating the presence of some secondary structure in the RNAT at the experimental temperature (37 °C). We showed (vide supra) that incorporation of the U46A mutation reduces prfA RNAT structural stability by 5.3 kcal/mol (Table 1) and found that prfA-U46A significantly upregulates (78% of control) GFP expression, consistent with previous studies.²⁰ Interestingly, our results show that mutations that stabilize regions proximal to the RBS (3C and L2_{stab}) and AUG (L1_{stab}) all reduce GFP expression to a similar extent (GFP expression of 5%, 5%, and 9% relative to the control, respectively). These results indicate that secondary structure formation around the RBS and AUG start codon negatively impacts gene expression, in agreement with previous studies. 20, 50

In addition to characterizing the impact of mutations proximal to the regions of the RNA that are important for translation (the RBS and AUG), we investigated sites distal to these regions. GFP reporter assays demonstrate that stabilization of the top part of the RNAT (prfA-L5_{stab}) reduced GFP expression by half compared to -WT (14% of control, **Fig. 7a**). Destabilization of the H4 helix (C58G and H4_{destab}) resulted in increased GFP expression (39% and 82% of control, respectively, **Fig. 7a**). These data clearly

indicate that regions distal to the RBS and the start codon play a significant role in the temperature-regulated control of gene translation. A comparison of GFP expression and the stabilizing effect of a particular mutation, as encoded in $\Delta\Delta G_{total}$ (**Table 1**), shows a positive linear correlation ($R_{Spearman} = 0.8862$, p = 0.0061) whereby stabilizing mutations reduce GFP expression and destabilizing mutations increase GFP expression, regardless of their location within the RNAT (**Fig. 7b**).

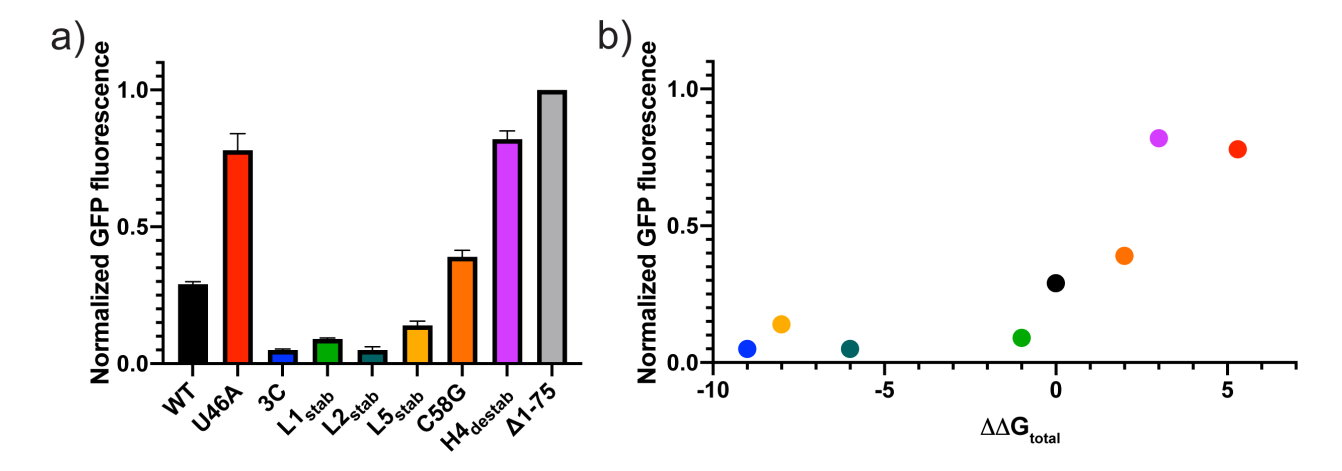


Figure 7. Translational control of GFP expression by various prfA RNAT derivatives. (a) Normalized GFP expression in *E. coli* containing either WT or mutant prfA RNAT elements in the 5' UTR. GFP expression levels in bacteria cultured at 37 °C are plotted relative to the positive control, prfA- Δ 1-75. Error bars indicate the standard deviation of three independent replicates. (b) Normalized GFP expression of prfA derivatives plotted against the $\Delta\Delta$ Gtotal for RNAT unfolding. Each RNAT construct is colored as in (a). Statistical significance was determined using a two-tailed Spearman correlation test, $R_{Spearman} = 0.8862$, p = 0.0061.

Discussion

RNA unfolding is a ubiquitous process that is required for a variety of macromolecular recognition events. RNA structure can be modulated by a variety of stimuli including ions,⁵¹ metabolites,⁵² pH,⁸ small- and macro-molecule binding,⁵³⁻⁵⁵ and temperature.⁵⁶ The structural plasticity of RNA allows for precise regulation in the face of changing environmental conditions. In order to gain further insight on the regulatory mechanisms of RNAs we must understand their structural stability and transitions on a

molecular level. RNATs provide a unique system for probing the molecular mechanisms that govern RNA unfolding in the absence of ligand binding events.

We began our analysis by comparing the melting of the prfA and cssA RNATs, two RNATs reported to draw on different mechanisms in their thermal response. A previous study of the cssA RNAT observed one primary unfolding transition (T_{m1} = 40.6 °C) with a presumed dimer unfolding transition at a much higher temperature (T_{m2} = 71 °C). In our hands, the cssA RNAT unfolds with a predominant single transition and the high temperature dimer unfolding event is a minor species, detectable only in our DSC data (Fig. 1d, Fig. S3). The differences in observed melting profile could be due to the use of RNAs that have slightly different sequences at the 5'-end⁵⁷ or the different solution conditions (ionic strength and pH). Similar to results reported for both the *Salmonella* 4U RNAT⁵⁸ and the *B. japonicum* ROSE RNAT, we found that addition of magnesium chloride significantly stabilized both the prfA and cssA RNATs in vitro and therefore the intracellular Mg²⁺ concentration may impact translation in vivo. Our studies show that prfA RNAT melting has two distinct unfolding transitions (Fig. 1), which implies presence of an intermediate conformation in the prfA RNAT unfolding process. These results confirm that the cssA and prfA RNAT unfolding occur via distinct mechanisms.

To further examine the sequence and structural features that contribute to the unfolding mechanism, we characterized a series of mutations designed to either stabilize or destabilize specific regions of the RNAT. Our results are consistent with a model in which the two observed transitions for the WT prfA RNAT report on unfolding events that take place in distinct regions of the RNAT. To illustrate, mutants designed to destabilize the H3 (U46A) and H4 elements (C58G and H4_{destab}) affect the main unfolding transition (T_{m1}) whereas the second transition remains largely unchanged (**Figs. 2,5**). We therefore posit that the first unfolding event reports primarily on the unfolding of the upper portion of the RNAT. However, our data also indicate that the unfolding events are not entirely independent of each other. Mutations designed to stabilize the L3 and L5 regions (3C and L5_{stab}, respectively) affect the thermal stability of both transitions. For the prfA-3C RNAT (**Fig. 2e**), the melting temperature of the main transition (transition 2) is highly cooperative and significantly stabilized relative to WT. Furthermore, the

minor transition (transition 1) is slightly destabilized. We attribute this increased cooperativity and stability to the elimination of L3, effectively lengthening the H3 helix. Elimination of L5 (prfA-L5_{stab}) results in an increase in the melting temperature of the first transition, but also stabilizes the subsequent unfolding event (**Fig. 4**). In both cases, the observed increased stability of the main unfolding transition is expected, as these mutations stabilize the H3/H4/H5 region. However, the effect that these mutations have on the minor transitions are unexpected, and suggestive of communication between the top and bottom regions of the RNAT.

To more completely assign the observed unfolding transitions to specific RNA structures, we examined the prfA RNAT structure using NMR spectroscopy. We identified spectroscopic probes that report on the base pairing of unique sequences within three different regions of the prfA RNAT (H3, H4, and H5; **Fig. 6**) at low temperature. As the temperature was increased, both chemical shift perturbations and line broadening were observed, suggesting that these regions of the RNAT melt in the first transition.

Furthermore, the stabilization of the L1 and L2 elements (L1_{stab} and L2_{stab}, respectively) display a distinct unfolding profile relative to the WT prfA RNAT. L1_{stab} and L2_{stab} are characterized by a single predominant unfolding event (**Fig. 3**). We postulate two plausible explanations for this observation. First, the L1_{stab} and L2_{stab} RNAT constructs have an increased T_m for the first transition with an apparent loss of the second transition. Alternatively, the unfolding profile is dominated by the "second" unfolding transition while the "first" unfolding event is in fact eliminated; i.e. the first and second transitions are occurring simultaneously. Both hypotheses are consistent with increased cooperativity between the two unfolding events. Although our data cannot directly discern between the two models, when viewed in conjunction with the other mutational analysis, the latter fits well with a model in which the upper regions unfold first and the lower regions unfold second. Further analysis of the thermodynamic values (**Table 1**) reveals a large difference in ΔH_1 between these two constructs. This difference is likely due to the formation of a largely extended base paired structure formed by the elimination of L2 (L2_{stab}) relative to the more isolated changes with partial stabilization of L1 (L1_{stab}).

Analysis of the thermal unfolding by both CD spectroscopy and DSC gives distinct insight into the RNA structures unfolding in each transition. CD (monitored at 260 nm) reports on the unfolding of the Ahelical structures, while DSC accounts for the energy associated with destabilization of helical and other structures. 30, 31 The energetics underlying the cssA melting are consistent when compared across methods (Tables S3 and 2), owing to the largely A-helical structure of this RNAT. Upon examination of the prfA RNATs, we noticed a striking difference. The energetics for the main transition (the first transition for prfA-WT) are generally consistent across methods, albeit the differences fall outside of the error of the measurement, suggesting that there are small, but real differences in the data, which we attribute to differences in structure in this region of the RNATs. However, the energetics for the minor transition (the second transition for prfA-WT) are notably different between methods. The enthalpy change for the minor transition, as measured by DSC, is significantly larger than the value obtained by fitting the CD data. We attribute these findings to the fact that the main transition involves unfolding of the largely Ahelical region near the top of the prfA RNAT (helix H3 to the apical loop). The second transition, which has a smaller enthalpy change when monitored by CD than DSC, corresponds the unfolding of A-helical elements H1 and H2, but also the large internal loops L1 and L2. We suspect that the large internal loops have some non-canonical structure that upon melting, contribute to the enthalpic value measured by DSC.

While the size of the RNA and severe chemical shift overlap precludes the ability to unambiguously identify each signal, qualitative insight into the structural changes by NMR is still possible. Examination of 1D imino proton spectra for the WT prfA RNAT and the mutants described in this study reveal chemical shift perturbations that are largely consistent with local structural changes (**Fig. S8**). Interestingly, for the H4_{destab} construct, which should disrupt one U•G and three G-C base pairs, we observe additional signals between 10-11 ppm. This is potentially consistent with the formation of G-G base pairs, which could partially stabilize this region. If correct, this helps to explain the striking similarities in the structural stability of the C58G single point mutation and the more extensive H4_{destab} mutation.

In addition to studying the effect of different mutations on the stability of prfA RNAT structure, we also evaluated how those mutations affect the temperature-regulated control of downstream gene expression (Fig. 7). Relative gene expression in the context of prfA-U46A and -3C RNATs are consistent with previous studies. ^{20, 24} Additionally, we showed mutations that stabilize internal loops both proximal to (L1_{stab} and L2_{stab}) and distal to (L5_{stab}) the AUG start codon and RBS display reduced GFP expression. Similarly, destabilizing mutations distal to the AUG start codon and RBS enhance GFP expression (C58G and H4_{destab}). Overall, we see a strong correlation between the stability of the RNA structure and GFP expression (Fig. 7b). In this analysis, prfA-C58G is the clear outlier. While this mutation was designed to disrupt only a single base pair, the measured thermodynamic stability is almost identical to the -H4_{destab} construct which harbors more extensive mutations in the same region. In the present study, we cannot rule out that the C58G mutation does not further disrupt the secondary structure. It is also possible that thermodynamics do not tell the whole story and that the kinetics of RNA folding and/or translation also play a significant role in the function of the RNAT.

While the architecture of the prfA RNAT is unique among known families of RNATs, the unfolding mechanism is reminiscent of other known RNATs. The unfolding of the cssA RNAT is known to initiate near the apical loop and continue down through the RBS.²² A similar mechanism has also been described for the *B. japonicum* ROSE RNAT.⁶⁰ The ROSE RNAT melts in a cooperative manner, first near the RBS, which is located at the apical loop, before the base of the helix melts.⁶⁰ Our results are also consistent with unfolding that is initiated at the regions proximal to the apical loop. What is unique is our observation of two distinct unfolding transitions, which we believe is a function of the RNAT structure. The thermosensing domain of the ROSE RNAT is significantly smaller than the prfA RNAT, and melts in a highly cooperative manner, likely due to the presence of canonical base pairing and the lack of large internal loops. The cssA RNAT, which also melts with high cooperativity, is more similar in size to the prfA RNAT. However, the cssA RNAT and prfA RNAT have very different secondary structures (Fig. 1), which we believe contributes to their unique mechanisms. The cssA RNAT contains few internal loops,

with 70% of the nucleotides in this RNAT engaged in base pairing in its "folded" state while only 58% of nucleotides are base paired in the prfA RNAT.

Internal loops play a central role in the precise functioning of RNATs. For example, in the *hsp17* RNAT, substitution of an internal loop near the RBS with a stabilizing base pair increased the thermal stability of the RNAT structure and reduced downstream gene expression. In the present study, we found that stabilizing or reducing the size of internal loops near the RBS of the prfA RNAT has a similar effect on RNA structural stability and downstream gene expression. Moreover, our results with the prfA-L5_{stab} RNAT (**Figs. 4,6**) indicate that internal loops distal to the RBS also have significant effects on overall RNAT structural stability and temperature control.

Conclusions

The data presented in this study provide further evidence in support of the model in which the cssA and prfA RNATs exert translational control via distinct mechanisms. Additionally, we demonstrate that in the absence of ribosome binding, the prfA RNAT unfolds in a pseudo-sequential mechanism in which the "top" of the prfA RNAT, near the apical loop, unfolds first followed by unfolding of the "bottom" of the RNAT, including the helical regions below the RBS and AUG start codon. We posit that during translation, it is the first unfolding event that drives ribosome binding and subsequent translation. However, our data also show that stabilization of the internal loops at the base of the RNAT (L1 and L2) has profound effects on the overall melting profile. RNA folding is a complex sequence-dependent mechanism, thereby limiting our ability to extract precise folding landscapes from energetics alone. However, these studies challenge the paradigm that local structure and thermal stability define RNAT function. We show that stabilization of regions distal to the RBS have profound effects on both the unfolding profile and translatability of the downstream message. Further structural, mutational, and biochemical studies will be necessary to illuminate the unfolding landscape of the prfA RNAT. This study provides a first step toward a mechanistic understanding of the molecular determinants of temperature-dependent prfA RNAT unfolding.

Acknowledgements

This work was supported by National Science Foundation grant MCB-1942398 and by funds from the

University of Michigan Biophysics Program and Department of Chemistry. This research used equipment

from the UM Biophysics Program Shared Research Resources. We would like to thank Dr. Joseph

Schauerte for providing training on and maintenance of the shared equipment. The authors would like to

acknowledge Dr. Anita Kotar for helpful discussions. Research reported in this publication was supported

by the University of Michigan BioNMR Core Facility (U-M BioNMR). U-M BioNMR Core is grateful

for support from U-M including the College of Literature, Sciences and Arts, Life Sciences Institute,

College of Pharmacy and the Medical School along with the U-M Biosciences Initiative. This study made

use of the National Magnetic Resonance Facility at Madison, which is supported by NIH grant

P41GM103399 (NIGMS), old number: P41RR002301. Equipment was purchased with funds from the

University of Wisconsin-Madison, the NIH P41GM103399, S10RR02781, S10RR08438, S10RR023438,

S10RR025062, S10RR029220), the NSF (DMB-8415048, OIA-9977486, BIR-9214394), and the USDA.

Supporting Information

Supporting information is available free of charge.

Equations for fitting CD and DSC data.

Table S1-S4.

Figures S1-S8.

Supplemental References.

30

References

- [1] Mignone, F., Gissi, C., Liuni, S., and Pesole, G. (2002) Untranslated regions of mRNAs, *Genome Biol* 3, REVIEWS0004, 1-10.
- [2] Yang, D., and Leibowitz, J. L. (2015) The structure and functions of coronavirus genomic 3' and 5' ends, *Virus Res* 206, 120-133.
- [3] Mayr, C. (2017) Regulation by 3'-Untranslated Regions, Annu Rev Genet 51, 171-194.
- [4] Schuster, S. L., and Hsieh, A. C. (2019) The Untranslated Regions of mRNAs in Cancer, *Trends Cancer* 5, 245-262.
- [5] Narberhaus, F., Waldminghaus, T., and Chowdhury, S. (2006) RNA thermometers, *FEMS Microbiol Rev* 30, 3-16.
- [6] Serganov, A., and Patel, D. J. (2007) Ribozymes, riboswitches and beyond: regulation of gene expression without proteins, *Nat Rev Genet* 8, 776-790.
- [7] Garst, A. D., Edwards, A. L., and Batey, R. T. (2011) Riboswitches: structures and mechanisms, *Cold Spring Harb Perspect Biol* 3:a003533, 1-13.
- [8] Houck-Loomis, B., Durney, M. A., Salguero, C., Shankar, N., Nagle, J. M., Goff, S. P., and D'Souza, V. M. (2011) An equilibrium-dependent retroviral mRNA switch regulates translational recoding, *Nature* 480, 561-564.
- [9] Breaker, R. R. (2012) Riboswitches and the RNA world, *Cold Spring Harb Perspect Biol 4:a003566*, 1-15.
- [10] Loh, E., Righetti, F., Eichner, H., Twittenhoff, C., and Narberhaus, F. (2018) RNA Thermometers in Bacterial Pathogens, *Microbiol Spectr* 6(2):RWR-0012-2017, 1-16.
- [11] Morita, M. T., Tanaka, Y., Kodama, T. S., Kyogoku, Y., Yanagi, H., and Yura, T. (1999) Translational induction of heat shock transcription factor sigma32: evidence for a built-in RNA thermosensor, *Genes Dev 13*, 655-665.
- [12] Loh, E., Kugelberg, E., Tracy, A., Zhang, Q., Gollan, B., Ewles, H., Chalmers, R., Pelicic, V., and Tang, C. M. (2013) Temperature triggers immune evasion by Neisseria meningitidis, *Nature* 502, 237-240.
- [13] Nocker, A., Hausherr, T., Balsiger, S., Krstulovic, N. P., Hennecke, H., and Narberhaus, F. (2001) A mRNA-based thermosensor controls expression of rhizobial heat shock genes, *Nucleic Acids Res* 29, 4800-4807.
- [14] Nocker, A., Krstulovic, N. P., Perret, X., and Narberhaus, F. (2001) ROSE elements occur in disparate rhizobia and are functionally interchangeable between species, *Arch Microbiol* 176, 44-51.
- [15] Waldminghaus, T., Fippinger, A., Alfsmann, J., and Narberhaus, F. (2005) RNA thermometers are common in alpha- and gamma-proteobacteria, *Biol Chem 386*, 1279-1286.
- [16] Waldminghaus, T., Heidrich, N., Brantl, S., and Narberhaus, F. (2007) FourU: a novel type of RNA thermometer in Salmonella, *Mol Microbiol* 65, 413-424.
- [17] Kouse, A. B., Righetti, F., Kortmann, J., Narberhaus, F., and Murphy, E. R. (2013) RNA-mediated thermoregulation of iron-acquisition genes in Shigella dysenteriae and pathogenic Escherichia coli, *PLoS One 8*, e63781, 1-13.
- [18] Bohme, K., Steinmann, R., Kortmann, J., Seekircher, S., Heroven, A. K., Berger, E., Pisano, F., Thiermann, T., Wolf-Watz, H., Narberhaus, F., and Dersch, P. (2012) Concerted actions of a thermo-labile regulator and a unique intergenic RNA thermosensor control Yersinia virulence, *PLoS Pathog 8*, e1002518, 1-23.
- [19] Chakraborty, T., Leimeister-Wachter, M., Domann, E., Hartl, M., Goebel, W., Nichterlein, T., and Notermans, S. (1992) Coordinate regulation of virulence genes in Listeria monocytogenes requires the product of the prfA gene, *J Bacteriol* 174, 568-574.

- [20] Johansson, J., Mandin, P., Renzoni, A., Chiaruttini, C., Springer, M., and Cossart, P. (2002) An RNA thermosensor controls expression of virulence genes in Listeria monocytogenes, *Cell* 110, 551-561.
- [21] de las Heras, A., Cain, R. J., Bielecka, M. K., and Vazquez-Boland, J. A. (2011) Regulation of Listeria virulence: PrfA master and commander, *Curr Opin Microbiol* 14, 118-127.
- [22] Barnwal, R. P., Loh, E., Godin, K. S., Yip, J., Lavender, H., Tang, C. M., and Varani, G. (2016) Structure and mechanism of a molecular rheostat, an RNA thermometer that modulates immune evasion by Neisseria meningitidis, *Nucleic Acids Res* 44, 9426-9437.
- [23] Konkel, M. E., and Tilly, K. (2000) Temperature-regulated expression of bacterial virulence genes, *Microbes Infect* 2, 157-166.
- [24] Neupert, J., Karcher, D., and Bock, R. (2008) Design of simple synthetic RNA thermometers for temperature-controlled gene expression in Escherichia coli, *Nucleic Acids Res 36*, e124, 1-9.
- [25] Cunningham, P. R., and Ofengand, J. (1990) Use of inorganic pyrophosphatase to improve the yield of in vitro transcription reactions catalyzed by T7 RNA polymerase, *Biotechniques 9*, 713-714.
- [26] Helmling, C., Keyhani, S., Sochor, F., Furtig, B., Hengesbach, M., and Schwalbe, H. (2015) Rapid NMR screening of RNA secondary structure and binding, *J Biomol NMR* 63, 67-76.
- [27] Buchmueller, K. L., and Weeks, K. M. (2004) Tris-borate is a poor counterion for RNA: a cautionary tale for RNA folding studies, *Nucleic Acids Res* 32, e184, 1-6.
- [28] Johnson, B. A., and Blevins, R. A. (1994) NMR View: A computer program for the visualization and analysis of NMR data, *J Biomol NMR 4*, 603-614.
- [29] Norris, M., Fetler, B., Marchant, J., and Johnson, B. A. (2016) NMRFx Processor: a cross-platform NMR data processing program, *J Biomol NMR 65*, 205-216.
- [30] Kypr, J., Kejnovská, I., Bednářová, K., and Vorlíčková, M. (2012) Circular dichroism spectroscopy of nucleic acids, In *Comprehensive Chiroptical Spectroscopy: Applications in Stereochemical Analysis of Synthetic Compounds, Natural Products, and Biomolecules, Volume 2* (Berova, N., Polavarapu, P. L., and Woody, R. W., Eds.), pp 575-586.
- [31] Gill, P., Moghadam, T. T., and Ranjbar, B. (2010) Differential scanning calorimetry techniques: applications in biology and nanoscience, *J Biomol Tech 21*, 167-193.
- [32] Biltonen, R. L., and Lichtenberg, D. (1993) The Use of Differential Scanning Calorimetry as a Tool to Characterize Liposome Preparations, *Chem Phys Lipids* 64, 129-142.
- [33] Chiu, M. H., and Prenner, E. J. (2011) Differential scanning calorimetry: An invaluable tool for a detailed thermodynamic characterization of macromolecules and their interactions, *J Pharm Bioallied Sci* 3, 39-59.
- [34] Misra, V. K., and Draper, D. E. (2001) A thermodynamic framework for Mg2+ binding to RNA, *Proc Natl Acad Sci U S A* 98, 12456-12461.
- [35] Klein, D. J., Moore, P. B., and Steitz, T. A. (2004) The contribution of metal ions to the structural stability of the large ribosomal subunit, *RNA 10*, 1366-1379.
- [36] Bowman, J. C., Lenz, T. K., Hud, N. V., and Williams, L. D. (2012) Cations in charge: magnesium ions in RNA folding and catalysis, *Curr Opin Struct Biol* 22, 262-272.
- [37] Watts, J. K., Martin-Pintado, N., Gomez-Pinto, I., Schwartzentruber, J., Portella, G., Orozco, M., Gonzalez, C., and Damha, M. J. (2010) Differential stability of 2'F-ANA*RNA and ANA*RNA hybrid duplexes: roles of structure, pseudohydrogen bonding, hydration, ion uptake and flexibility, *Nucleic Acids Res* 38, 2498-2511.
- [38] Chen, Z., and Znosko, B. M. (2013) Effect of sodium ions on RNA duplex stability, *Biochemistry 52*, 7477-7485.
- [39] Wadkins, T. S., Shih, I., Perrotta, A. T., and Been, M. D. (2001) A pH-sensitive RNA tertiary interaction affects self-cleavage activity of the HDV ribozymes in the absence of added divalent metal ion, *J Mol Biol* 305, 1045-1055.
- [40] Römer, R., and Hach, R. (1975) tRNA conformation and magnesium binding. A study of a yeast phenylalanine-specific tRNA by a fluorescent indicator and differential melting curves, *Eur J Biochem* 55, 271-284.

- [41] Stein, A., and Crothers, D. M. (1976) Equilibrium binding of magnesium(II) by Escherichia coli tRNAfMet, *Biochemistry 15*, 157-160.
- [42] Barton, S., Heng, X., Johnson, B. A., and Summers, M. F. (2013) Database proton NMR chemical shifts for RNA signal assignment and validation, *J Biomol NMR* 55, 33-46.
- [43] Kotar, A., Foley, H. N., Baughman, K. M., and Keane, S. C. (2020) Advanced approaches for elucidating structures of large RNAs using NMR spectroscopy and complementary methods, *Methods*, 1-15.
- [44] Lu, K., Heng, X., Garyu, L., Monti, S., Garcia, E. L., Kharytonchyk, S., Dorjsuren, B., Kulandaivel, G., Jones, S., Hiremath, A., Divakaruni, S. S., LaCotti, C., Barton, S., Tummillo, D., Hosic, A., Edme, K., Albrecht, S., Telesnitsky, A., and Summers, M. F. (2011) NMR detection of structures in the HIV-1 5'-leader RNA that regulate genome packaging, *Science 334*, 242-245.
- [45] Tran, T., Liu, Y., Marchant, J., Monti, S., Seu, M., Zaki, J., Yang, A. L., Bohn, J., Ramakrishnan, V., Singh, R., Hernandez, M., Vega, A., and Summers, M. F. (2015) Conserved determinants of lentiviral genome dimerization, *Retrovirology* 12, 83, 1-16.
- [46] Cornilescu, G., Didychuk, A. L., Rodgers, M. L., Michael, L. A., Burke, J. E., Montemayor, E. J., Hoskins, A. A., and Butcher, S. E. (2016) Structural Analysis of Multi-Helical RNAs by NMR-SAXS/WAXS: Application to the U4/U6 di-snRNA, *J Mol Biol 428*, 777-789.
- [47] Keane, S. C., Van, V., Frank, H. M., Sciandra, C. A., McCowin, S., Santos, J., Heng, X., and Summers, M. F. (2016) NMR detection of intermolecular interaction sites in the dimeric 5'-leader of the HIV-1 genome, *Proc Natl Acad Sci U S A 113*, 13033-13038.
- [48] Kranawetter, C., Brady, S., Sun, L., Schroeder, M., Chen, S. J., and Heng, X. (2017) Nuclear Magnetic Resonance Study of RNA Structures at the 3'-End of the Hepatitis C Virus Genome, *Biochemistry* 56, 4972-4984.
- [49] Marchant, J., Bax, A., and Summers, M. F. (2018) Accurate Measurement of Residual Dipolar Couplings in Large RNAs by Variable Flip Angle NMR, *J Am Chem Soc 140*, 6978-6983.
- [50] Cimdins, A., Klinkert, B., Aschke-Sonnenborn, U., Kaiser, F. M., Kortmann, J., and Narberhaus, F. (2014) Translational control of small heat shock genes in mesophilic and thermophilic cyanobacteria by RNA thermometers, *RNA Biol* 11, 594-608.
- [51] Draper, D. E. (2004) A guide to ions and RNA structure, RNA 10, 335-343.
- [52] Roth, A., and Breaker, R. R. (2009) The structural and functional diversity of metabolite-binding riboswitches, *Annu Rev Biochem* 78, 305-334.
- [53] Ganser, L. R., Kelly, M. L., Patwardhan, N. N., Hargrove, A. E., and Al-Hashimi, H. M. (2020) Demonstration that Small Molecules can Bind and Stabilize Low-abundance Short-lived RNA Excited Conformational States, *J Mol Biol* 432, 1297-1304.
- [54] Grossoehme, N. E., Li, L., Keane, S. C., Liu, P., Dann, C. E., 3rd, Leibowitz, J. L., and Giedroc, D. P. (2009) Coronavirus N protein N-terminal domain (NTD) specifically binds the transcriptional regulatory sequence (TRS) and melts TRS-cTRS RNA duplexes, *J Mol Biol 394*, 544-557.
- [55] Woodson, S. A., Panja, S., and Santiago-Frangos, A. (2018) Proteins That Chaperone RNA Regulation, *Microbiol Spectr* 6, 1-13.
- [56] Kortmann, J., and Narberhaus, F. (2012) Bacterial RNA thermometers: molecular zippers and switches, *Nat Rev Microbiol* 10, 255-265.
- [57] Kharytonchyk, S., Monti, S., Smaldino, P. J., Van, V., Bolden, N. C., Brown, J. D., Russo, E., Swanson, C., Shuey, A., Telesnitsky, A., and Summers, M. F. (2016) Transcriptional start site heterogeneity modulates the structure and function of the HIV-1 genome, *Proc Natl Acad Sci U S A 113*, 13378-13383.
- [58] Rinnenthal, J., Klinkert, B., Narberhaus, F., and Schwalbe, H. (2011) Modulation of the stability of the Salmonella fourU-type RNA thermometer, *Nucleic Acids Res* 39, 8258-8270.
- [59] Chowdhury, S., Maris, C., Allain, F. H., and Narberhaus, F. (2006) Molecular basis for temperature sensing by an RNA thermometer, *EMBO J 25*, 2487-2497.
- [60] Chowdhury, S., Ragaz, C., Kreuger, E., and Narberhaus, F. (2003) Temperature-controlled structural alterations of an RNA thermometer, *J Biol Chem* 278, 47915-47921.

- [61] Kortmann, J., Sczodrok, S., Rinnenthal, J., Schwalbe, H., and Narberhaus, F. (2011) Translation on demand by a simple RNA-based thermosensor, *Nucleic Acids Res* 39, 2855-2868.
- [62] Tostesen, E., Chen, S. J., and Dill, K. A. (2001) RNA folding transitions and cooperativity, *Journal of Physical Chemistry B* 105, 1618-1630.

Supporting Information

A Tale of Two Transitions: The Unfolding Mechanism of the prfA RNA Thermosensor

Huaqun Zhang¹, Ian Hall², Amos J. Nissley², Kyrillos Abdallah^{1,2}, Sarah C. Keane^{1,2*}

¹ Biophysics Program, University of Michigan, Ann Arbor, Michigan 48109, United States

² Department of Chemistry, University of Michigan, Ann Arbor, Michigan 48109, United States

^{*} Corresponding author: sckeane@umich.edu

Equations for fitting CD data:

One-transition fitting model:

$$f(T) = (0.1 * A_1) * \left(H_1 \div \left(2 * R * \sqrt{T}\right)\right) \div \left(1 + \cosh\left(\frac{H_1}{R * T * Tm_1 * (T - Tm_1)}\right)\right)$$

Two-transition fitting model:

$$f(T) = (0.1 * A_1) * \left(H_1 \div \left(2 * R * \sqrt{T}\right)\right) \div \left(1 + \cosh\left(\frac{H_1}{R * T * T m_1 * (T - T m_1)}\right) + (0.1 * A_2) * \left(H_2 \div \left(2 * R * \sqrt{T}\right)\right) \div \left(1 + \cosh\left(\frac{H_2}{R * T * T m_2 * (T - T m_2)}\right)\right)$$

Where A_1 and A_2 represent the relative hyperchromicity (10X) of each unfolding transition, T is the temperature in Kelvin, Tm is the transition temperature in Kelvin, and H_1 and H_2 represent the enthalpy change for each transition (kcal/mol).

Analysis of ion dependence:

$$\Delta n_{ion} = 1.11 * \left(\frac{\Delta H_n}{R * \left(T_{m,n}^2\right)}\right) * \left(\frac{\delta T_{m,n}}{\delta (\ln[K^+])}\right)$$

Where $\delta T_{m,n}/\delta(\ln[K+])$ represents the slope of the $T_{m,n}$ versus $\ln[K^+]$ and R is the ideal gas constant.^{1, 2} Enthalpy values were determined as described above, by fitting the CD thermal denaturation data to a two-transition fitting model.

Equations for fitting DSC data:

Two-state scaled model:

$$C_P = (\Delta H * 1000)^2 / (R * T^2) * \frac{e^{\left(\Delta H * 1000 * \frac{-Tm + T}{Tm * T * R}\right)}}{\left(1 + e^{\left(-\Delta H * 1000 * \frac{1 - \frac{T}{Tm}}{R * T}\right)}\right)^2} * Aw$$

Where T is the temperature in Kelvin, Tm is the transition temperature in Kelvin, ΔH is the change in enthalpy (kcal/mol), R is the ideal gas constant, and Aw is a peak scaling factor. As appropriate, multiple two-state scaled models were used to fit the DSC data.

Table S1. Primers used for DNA amplification and mutagenesis in the study.

Primer name	Sequence ^{a,b}	Comment
	GGAATTGTGAGCGGATAACAATTTCACACAGG	Forward primer to amplify all prfA constructs DNA template for
pUC57-80_Fwd	AAAC	in-vitro transcription
		Reverse primer to amplify all prfA constructs DNA template for
HH-prfA_Rev	mUmUGAGCGTTCATGTCTCATCCCCC	in-vitro transcription
		Forward primer for site-directed mutagenesis to generate
prfA_T46A_Fwd	CAGCTAACAAaTGTTGTTACTG	pUC57-prfA-U46A and pBS SK(+)-prfA-U46A-GFP
		Reverse primer for site-directed mutagenesis to generate pUC57-
prfA_T46A_Rev	TTGAAAGAAAGTCACGCTAAAG	prfA-U46A and pBS SK(+)-prfA-U46A-GFP
prfA-		Forward primer for site-directed mutagenesis to generate
T40C/A41C/A42C_Fwd	TTTCAACAGCcccCAATTGTTGTTACTG	pUC57-prfA-3C and pBS SK(+)-prfA-3C-GFP
prfA-		Reverse primer for site-directed mutagenesis to generate pUC57-
T40C/A41C/A42C Rev	GAAAGTCACGCTAAAGAC	prfA-3C and pBS SK(+)-prfA-3C-GFP
	TTAGCGTGACcatgTTTCAACAGCTAACAATTGT	Forward primer for site-directed mutagenesis to generate
prfA-2629 Fwd	TGTTAC	pUC57-prfA-L1 _{stab}
		Reverse primer for site-directed mutagenesis to generate pUC57-
prfA-2629 Rev	AGACGGTACCGGGTACCG	prfA-L1 _{stab}
		Forward primer for site-directed mutagenesis to generate
prfA-3538 Fwd	CTTTCTTTCAtCTAACAATTGTTGTTACTGCC	pUC57-prfA-L2 _{stab}
		Reverse primer for site-directed mutagenesis to generate pUC57-
prfA-3538 Rev	TCACGCTAAAGACGGTAC	prfA-L2 _{stab}
print bobo_reev	GTTACTGCCTtTTTTTAGGGTATTTTAAAAAAG	Forward primer for site-directed mutagenesis to generate
prfA-6164T Fwd	G	pUC57-prfA-L5 _{stab} and pBS SK(+)-prfA- L5 _{stab} -GFP
pini oro ii_i wa		Reverse primer for site-directed mutagenesis to generate pUC57-
prfA-6164T Rev	AACAATTGTTAGCTGTTGAAAG	prfA-L5 _{stab} and pBS SK(+)-prfA- L5 _{stab} -GFP
pini oro ri_rev	TGTTGTTACTcgggAATGTTTTTAGGGTATTTTA	Forward primer for site-directed mutagenesis to generate
prfA-2629-5760 Fwd	AAAAAG	pUC57-prfA-H4 _{destab} and pBS SK(+)-prfA-H4 _{destab} -GFP
pini 2029 3700_1 wa	THERETO	Reverse primer for site-directed mutagenesis to generate pUC57-
prfA-5760 Rev	ATTGTTAGCTGTTGAAAGAAAG	prfA-H4 _{destab} and pBS SK(+)-prfA-H4 _{destab} -GFP
pini-3700_icev	MITGITAGETGITGAMAGAMAG	Forward primer for site-directed mutagenesis to generate
prfA-C58G Fwd	GTTGTTACTGgCTAATGTTTTTAG	pUC57-prfA-C58G and pBS SK(+)-prfA-C58G-GFP
priA-C38G_1 wu	GITGITACIGCIAATGITTITAG	Reverse primer for site-directed mutagenesis to generate pUC57-
prfA-C58G Rev	AATTGTTAGCTGTTGAAAG	prfA-C58G and pBS SK(+)-prfA-C58G-GFP
PBS-prfA Fwd	ATGTAGATCGGGAATTCGAGGAGCTCG	Forward primer to amplify gene block prfA-GFP for cloning
TBS-pHA_Fwu	AGTTAAAGTCTCGAAGCTTGATATCGAATTCA	Torward primer to ampirity gene block priA-Gr1 for clonning
DDC prfA Dov	ATGGAAGC	Reverse primer to amplify gene block prfA-GFP for cloning
PBS-prfA_Rev	ATOGAAGC	Forward primer for site-directed mutagenesis to generate pBS
pBS-prfA 2629 Fwd	TTAGCGTGACcatgTTTCAACAGCTAAC	SK(+)-prfA-L1 _{stab} -GFP
pbs-piiA_2029_FWU	TIAGCOTOACCAIGITICAACAGCTAAC	Reverse primer for site-directed mutagenesis to generate pBS
nDC nefA 2620 Dev	ATGATGTTTTTACAGGATCC	
pBS-prfA_2629_Rev	ATUATUTTTTTACAUGATCC	SK(+)-prfA-L1 _{stab} -GFP Forward primer for site-directed mutagenesis to generate pBS
"DC ""fA 2520 Ev-1		
pBS-prfA-3538_Fwd	CTTTCTTTCAtCTAACAATTGTTGTTACTGC	SK(+)-prfA-L2 _{stab} -GFP Reverse primer for site-directed mutagenesis to generate pBS
DC CA 2520 D	TC A CCCT A A A TC A TCTTTTT A C	Reverse primer for site-directed mutagenesis to generate pBS
pBS-prfA_3538_Rev	TCACGCTAAATGATGTTTTTTAC	SK(+)-prfA-L2 _{stab} -GFP
pBS-prfA_delat1-		Forward primer for site-directed mutagenesis to generate pBS
75_Fwd	TTTTAAAAAAGGGCGATAAAAAACGATTG	SK(+)-prfA-delta1-75-GFP
DDG CA 114' B	GG + TGG GT + TGG + + GG GG	Reverse primer for site-directed mutagenesis to generate pBS
PBS-prfA_deletion_Rev	GGATCCGTATCCAAGCGC	SK(+)-prfA-delta1-75-GFP

^a m denotes 2'-O-Me modification of the primer ^b Mutations are denoted in lowercase letters.

Table S2. Sequences of RNAT constructs used in this study.

RNAT name	Sequence $(5' \rightarrow 3')^a$
	AAUUUAUGAGUACGUAGAGUAUAAUUAGUAUUCUUCUUUCCAACUUCCUUAUACUUAUAUACU
cssA	UAUAGAUU
CA XXVIII	UUUAGCGUGACUUUCUUUCAACAGCUAACAAUUGUUGUUACUGCCUAAUGUUUUUUAGGGUAUU
prfA-WT	UUAAAAAAGGGCGAUAAAAAACGAUUGGGGGAUGAGACAUGAACGCUCAA
0. 77464	UUUAGCGUGACUUUCUUUCAACAGCUAACAAUaGUUGUUACUGCCUAAUGUUUUUUAGGGUAUU
prfA-U46A	UUAAAAAAGGGCGAUAAAAAACGAUUGGGGGAUGAGACAUGAACGCUCAA
	UUUAGCGUGACUUUCUUUCAACAGCeecCAAUUGUUGUUACUGCCUAAUGUUUUUAGGGUAUUU
prfA-3C	UAAAAAAGGGCGAUAAAAAACGAUUGGGGGAUGAGACAUGAACGCUCAA
0. 7.4	UUUAGCGUGACcaugUUUCAACAGCUAACAAUUGUUGUUACUGCCUAAUGUUUUUUAGGGUAUUU
prfA-L1 _{stab}	UAAAAAAGGGCGAUAAAAAACGAUUGGGGGAUGAGACAUGAACGCUCAA
Ct. T.O.	UUUAGCGUGACUUUCUUUCAuCUAACAAUUGUUGUUACUGCCUAAUGUUUUUAGGGUAUUUUA
prfA-L2 _{stab}	AAAAAGGGCGAUAAAAAACGAUUGGGGGAUGAGACAUGAACGCUCAA
24 7 7	UUUAGCGUGACUUUCUUUCAACAGCUAACAAUUGUUGUUACUGCCUuUUUUUUAGGGUAUUUUA
prfA-L5 _{stab}	AAAAAGGGCGAUAAAAAACGAUUGGGGGAUGAGACAUGAACGCUCAA
01 G#0G	UUUAGCGUGACUUUCUUUCAACAGCUAACAAUUGUUGUUACUGgCUAAUGUUUUUUAGGGUAUU
prfA-C58G	UUAAAAAAGGGCGAUAAAAAACGAUUGGGGGAUGAGACAUGAACGCUCAA
2	UUUAGCGUGACUUUCUUUCAACAGCUAACAAUUGUUGUUACUcgggAAUGUUUUUAGGGUAUUU
prfA-H4 _{destab}	UAAAAAAGGCCAUAAAAAACGAUUGGGGGAUGAGACAUGAACGCUCAA

^a Mutations are denoted in lowercase letters.

Table S3. Thermodynamic parameters for RNAT unfolding derived from CD data.

Construct	T _{m1}	ΔH_1	ΔS_1	$\Delta G^{\circ}{}_{1}$	T _{m2}	ΔH_2	ΔS_2	ΔG°_{2}	ΔG°_{total}	$\Delta\Delta G^{\circ}_{total}$
	(°C) ^a	(kcal/mol)a	[cal/(mol•K)]	(kcal/mol)a,b	(°C) ^a	(kcal/mol)a	[cal/(mol•K)]	(kcal/mol)a,	(kcal/mo	(kcal/mol)
			a				a	b	1) ^c	WT-mut ^d
cssA	36.1 ± 0.4	104 ± 7	340 ± 20	5.4 ± 0.2	n.d.	n.d.	n.d.	n.d.	n.d.	-
prfA-WT	37.2 ± 0.2	136 ± 4	440 ± 10	5.4 ± 0.2	44.0 ± 0.6	24.9 ± 0.6	78 ± 2	1.50 ± 0.02	6.9 ± 0.2	0
prfA-U46A	32.5 ± 0.2	122 ± 4	400 ± 10	3.0 ± 0.1	41.5 ± 0.8	23.4 ± 0.7	75 ± 2	1.24 ± 0.03	4.2 ± 0.1	2.7 ± 0.2
prfA-3C	43.2 ± 0.2	40 ± 1	125 ± 4	2.29 ± 0.08	56.8 ± 0.5	134 ± 4	410 ± 10	13.0 ± 0.4	15.3 ± 0.4	-8.4 ± 0.5
prfA-L1 _{stab}	45.3 ± 0.3	157.3 ± 0.5	494 ± 1	10.1 ± 0.2	52.2 ± 0.1	14.0 ± 0.6	43 ± 2	1.17 ± 0.05	11.3 ± 0.2	-4.4 ± 0.3
prfA-L2 _{stab}	44.5 ± 0.1	169 ± 2	532 ± 6	10.5 ± 0.2	47 ± 1	16 ± 3	51 ± 8	1.1 ± 0.1	11.6 ± 0.2	-4.7 ± 0.3
prfA-L5 _{stab}	40.1 ± 0.1	124 ± 5	400 ± 20	6.0 ± 0.2	45.8 ± 0.6	35.9 ± 0.4	113 ± 1	2.36 ± 0.08	8.4 ± 0.2	-1.5 ± 0.3
prfA-C58G	31.98 ± 0.08	129 ± 2	423 ± 7	3.02 ± 0.04	41.8 ± 0.6	22.2 ± 0.2	70.3 ± 0.6	1.19 ± 0.05	4.21 ± 0.06	2.7 ± 0.2
prfA-H4 _{destab}	32.4 ± 0.3	107 ± 3	350 ± 10	2.65 ± 0.03	41.5 ± 0.4	21.2 ± 0.1	67.3 ± 0.4	1.12 ± 0.02	3.77 ± 0.04	3.1 ± 0.2

n.d.: not determined

 $[^]aT_m,\,\Delta G^\circ,\,\Delta H,$ and ΔS values are represented as the average of three replicate measurements \pm the standard deviation

^bAt 25 °C.

 $^{^{}c}\Delta G^{\circ}_{total}$ is the sum of ΔG°_{1} and ΔG°_{2} . Error was propagated from the errors associated with ΔG°_{1} and ΔG°_{2} .

 $^{^{}d}\Delta\Delta G^{\circ}_{\text{total}}$ is defined as $\Delta G^{\circ}_{\text{total-WT}}$ - $\Delta G^{\circ}_{\text{total-mutant}}.$ Error was propagated from the errors associated with $\Delta G^{\circ}_{\text{total-WT}}$ and $\Delta G^{\circ}_{\text{total-mutant}}.$

Table S4. Full width half max (FWHM) measurements of RNAT unfolding derived from DSC data.

Construct	FWHM ₁ ^a	FWHM ₂ ^a	FWHM _{total} ^b	ΔFWHM ₁ ^e	ΔFWHM ₂ ^f	$\Delta FWHM_{total}{}^{g}$
cssA	5.2 ± 0.1	8.9 ± 0.3	11 ± 2	-0.1 ± 0.1	-7.2 ± 0.9	-9 ± 2
prfA WT	5.3 ± 0.1	16.1 ± 0.8	20.0 ± 0.4	1	1	-
prfA U46A°	6.7 ± 0.2	16.0 ± 0.6	25.2 ± 0.2	1.4 ± 0.2	0 ± 1	5.2 ± 0.4
prfA 3C ^c	10.6 ± 0.8	5.4 ± 0.2	22.5 ± 0.2	5.3 ± 0.8	-10.7 ± 0.8	2.5 ± 0.4
prfA L1 _{stab} ^d	3.9 ± 0.2	12 ± 2	12 ± 2	-1.4 ± 0.2	-4 ± 2	-8 ± 2
prfA L2 _{stab} ^d	4.1 ± 0.4	16 ± 3	16 ± 3	-1.2 ± 0.4	0 ± 3	-4 ± 3
prfA L5 _{stab} ^{c,h}	8.3 ± 0.2	9.7 ±0.7	19.4 ± 0.7	3.0 ± 0.2	-6 ± 1	-0.6 ± 0.8
prfA C58G ^c	5.79 ± 0.09	15.9 ± 0.2	24.52 ± 0.08	0.5 ± 0.1	-0.2 ± 0.8	4.5 ± 0.4
prfA H4 _{destab}	6.4 ± 0.2	17.9 ± 0.7	22.6 ± 0.7	1.1 ± 0.2	2 ± 1	2.6 ± 0.8

 $^{^{}a}$ Values of FWHM are represented as the average of three replicate measurements \pm the standard deviation.

^bFWHM_{total} is defined as the difference in falling edge (FE) of peak 2 and the rising edge (RE) of peak 1 (FE₂ – RE₁).

^cFWHM_{total} is defined as the sum of FWHM₁ and FWHM₂ when RE₂ is greater than FE₁.

^dFWHM_{total} value is defined as FWHM₂ because FWHM₂ covers the entire range of both transitions and FWHM₂ is greater than (FE₂-RE₁).

 $[^]e\Delta FWHM_1$ is defined as $FWHM_{1\ mutant}$ - $FWHM_{1\ WT}$. Associated error was propagated from the standard deviation of $FWHM_{1\ mutant}$ and $FWHM_{1\ WT}$.

 $^{^{\}rm f}\Delta FWHM_2$ is defined as $FWHM_2$ mutant - $FWHM_2$ WT. Associated error was propagated from the standard deviation of $FWHM_2$ mutant and $FWHM_2$ WT.

 $[^]g\Delta FWHM_{total}$ is defined as $FWHM_{total\ mutant}$ - $FWHM_{total\ WT}$. Associated error was propagated from the standard deviation of $FWHM_{total\ mutant}$ and $FWHM_{total\ WT}$.

^hprfA L5_{stab} values are based on two replicate measurements.

Table S5. T_m values determined at various concentrations of mono- and di-valent metal ions.

Construct	[K ⁺] (mM) ^a	$[Mg^{2+}] (mM)^a$	T _{ml} (°C) ^b	T _{m2} (°C) ^b
prfA-WT	67	0	37.0 ± 0.3	45 ± 2
	92	0	39.0 ± 0.4	46.2 ± 0.8
	117	0	40.6 ± 0.5	47.13 ± 0.09
	142	0	41.8 ± 0.3	48.0 ± 0.6
	167	0	43.1 ± 0.3	53 ± 1
	192	0	43.7 ± 0.4	50.7 ± 0.6
	67	0.2	38.38 ± 0.08	44.4 ± 0.3
	67	0.5	40.4 ± 0.6	45.8 ± 0.9
	67	1	43.1 ± 0.9	47.5 ± 0.7
	67	2	46 ± 2	50 ± 1
	67	5	51 ± 1	55 ± 2
cssA	67	0	36.2 ± 0.2	n.d.
	92	0	38.41 ± 0.09	n.d.
	117	0	40.1 ± 0.1	n.d.
	142	0	41.14 ± 0.03	n.d.
	167	0	42.08 ± 0.08	n.d.
	192	0	42.87 ± 0.02	n.d.
	67	0.2	37.8 ± 0.2	n.d.
	67	0.5	39.6 ± 0.4	n.d.
	67	1	41.8 ± 0.3	n.d.
	67	2	46.61 ± 0.05	n.d.
	67	5	48.1 ± 0.2	n.d.

n.d.: not determined

^aTotal ion concentration in solution. ^b T_m values are represented as the average of three replicate measurements \pm the standard deviation.

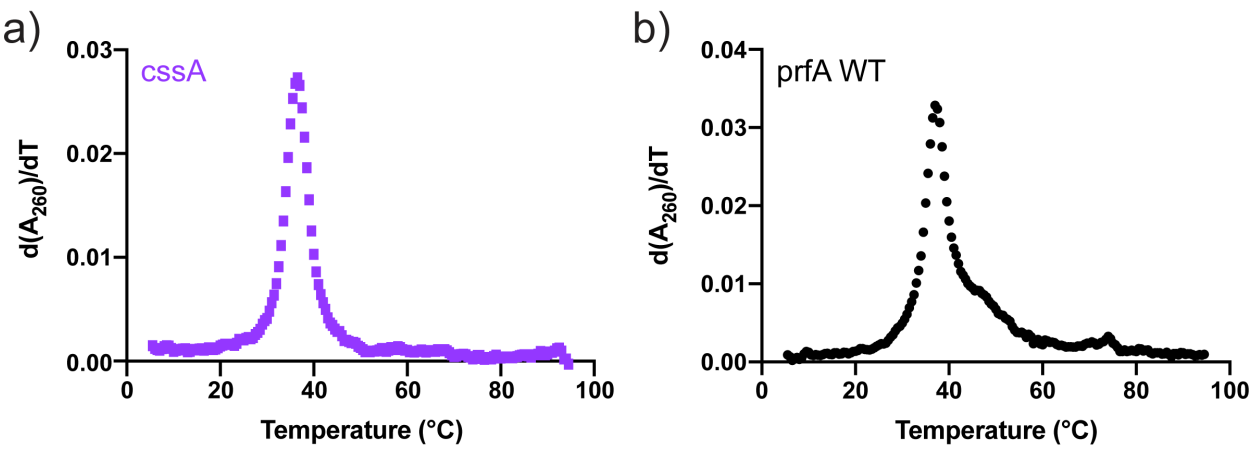


Figure S1. Thermal melting data of prfA and cssA RNATs by CD spectroscopy. Absorbance values at 260 nm (A260) were recorded along with CD and were used to calculate first derivatives for cssA (a) and prfA (b).

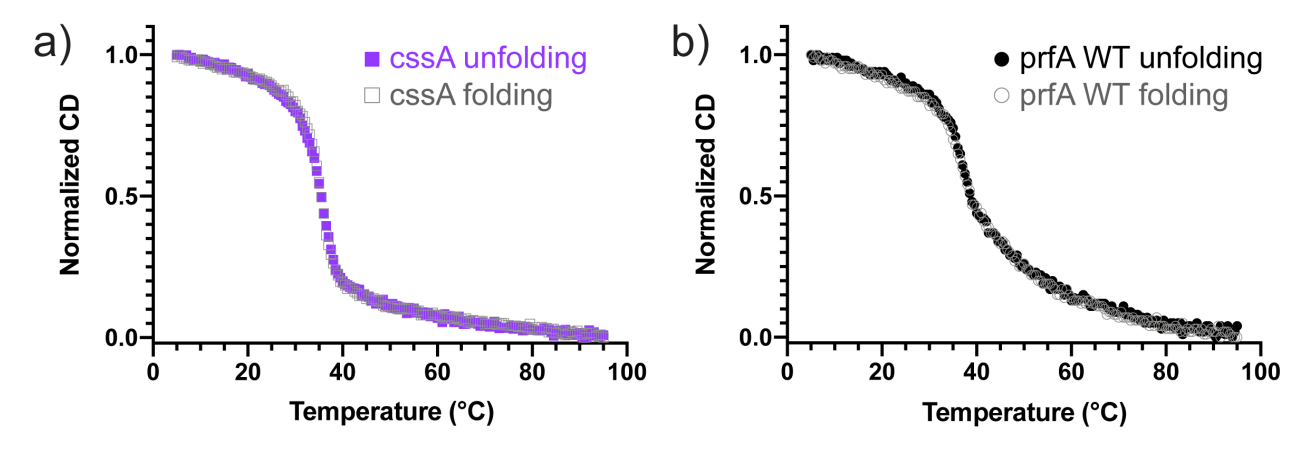


Figure S2. The cssA and prfA RNATs unfold in a reversible manner. Unfolding and folding spectra overlay of (a) cssA and (b) prfA RNATs. Data were normalized between 0 and 1 for comparison.

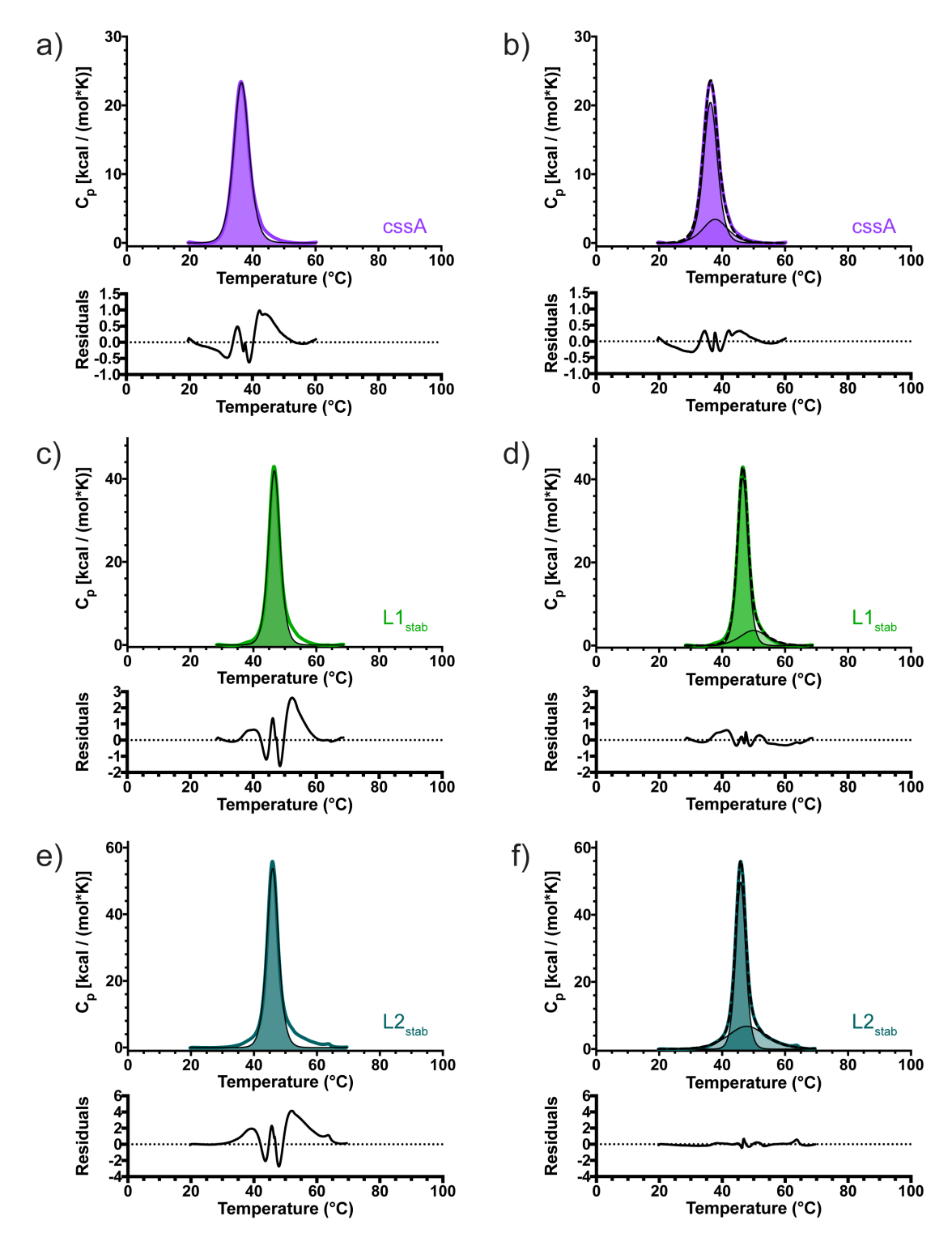


Figure S3. Comparison of one vs. two two-state scaled fitting model for DSC data. cssA (a, b), $prfA-L1_{stab}$ (c, d), and $prfA-L2_{stab}$ (e, f) RNAT elements that appeared to be fittable by a single two-state transition were analyzed both with a single two-state transition (a, c, and e) and two two-state transitions (b, d, f). Residual plots for each fit are shown below the DSC data.

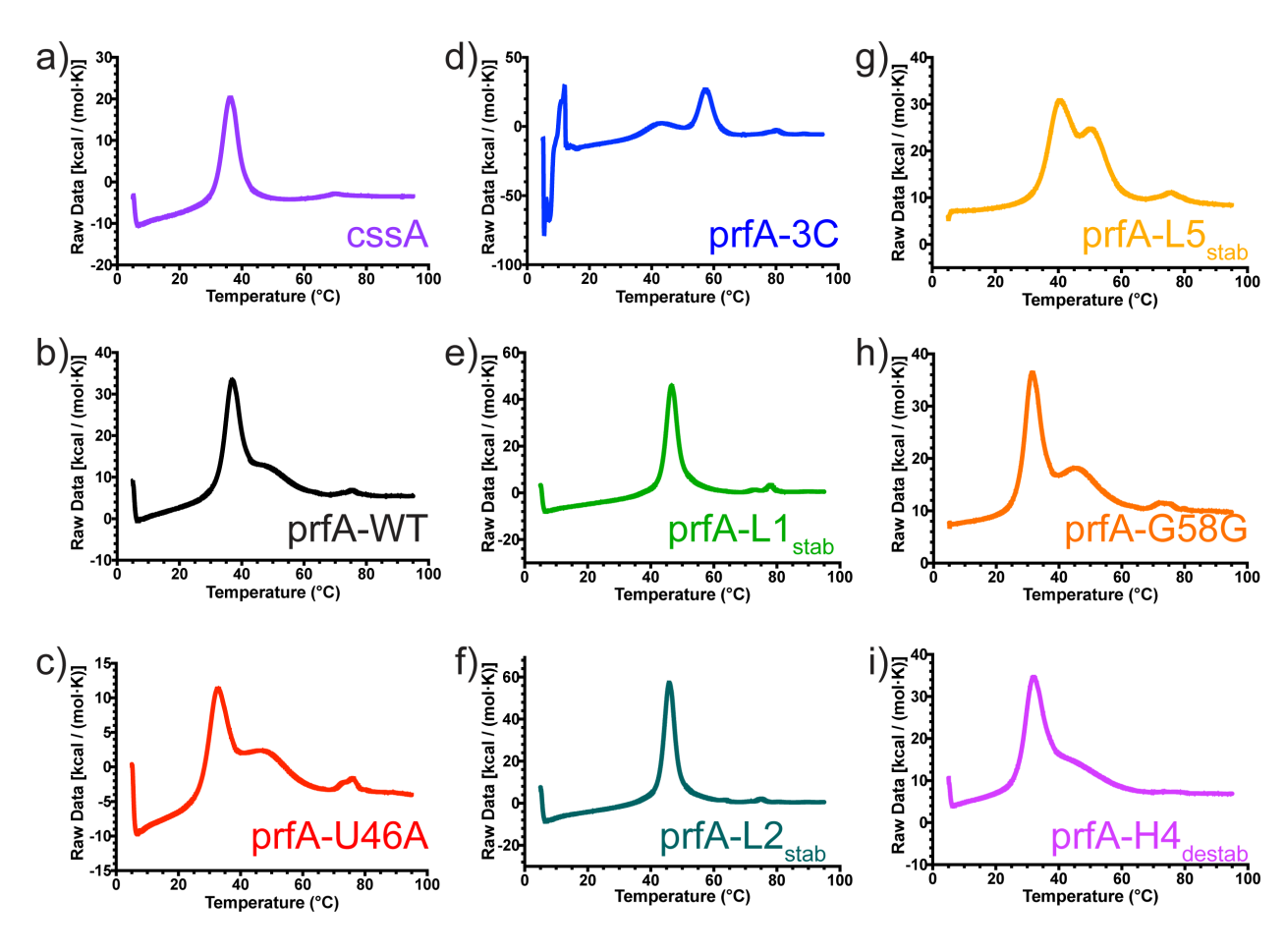


Figure S4. Raw DSC traces for constructs used in this study (a) cssA, (b) prfA-WT, (c) prfA-U46A, (d) prfA-3C, (e) prfA-L1_{stab}, (f) prfA-L2_{stab}, (g) prfA-L5_{stab}, (h) prfA-C58G, and (i) prfA-H4_{destab}.

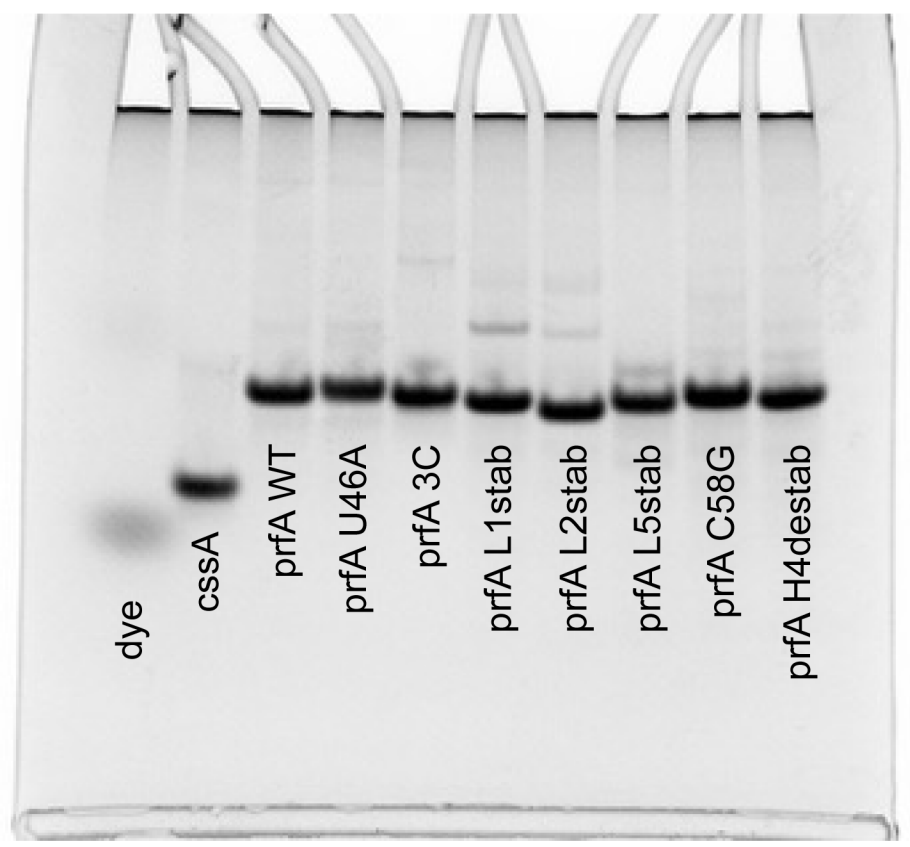


Figure S5. Native gel analysis of RNAT constructs used in this study.

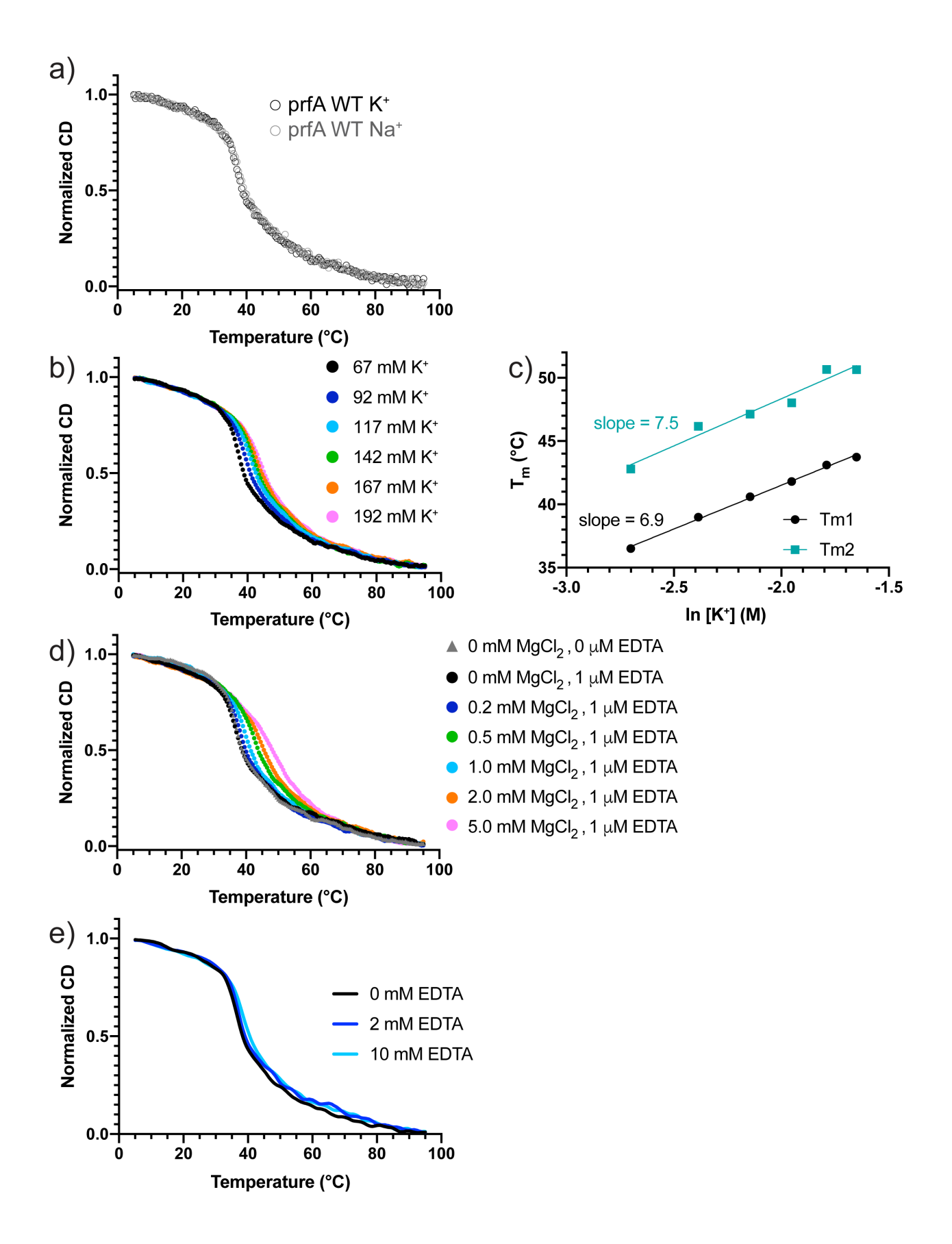


Figure S6. Thermal melting data of prfA under various ion conditions. (a) CD spectra overlay of prfA RNAT melting in Na $^+$ (50 mM Na_xH_yPO₄, pH 6.5) and K $^+$ (50 mM K_xH_yPO₄, pH 6.5) buffer. (b) Thermal denaturation experiments of the prfA RNAT with increasing concentration of KCl. Figure legend indicates the total concentration of K $^+$ in the buffer. (c) Plot of T_m vs. ln[K $^+$] to analyze the ion-dependence of unfolding. (d) Titration experiments of the prfA RNAT with MgCl₂. Figure legend indicates the concentrations of MgCl₂ and EDTA added to the standard phosphate buffer. (e) Thermal denaturation of prfA RNAT in the presence of high concentrations of EDTA. All CD data were monitored at 260 nm and normalized between 0 and 1 for comparison.

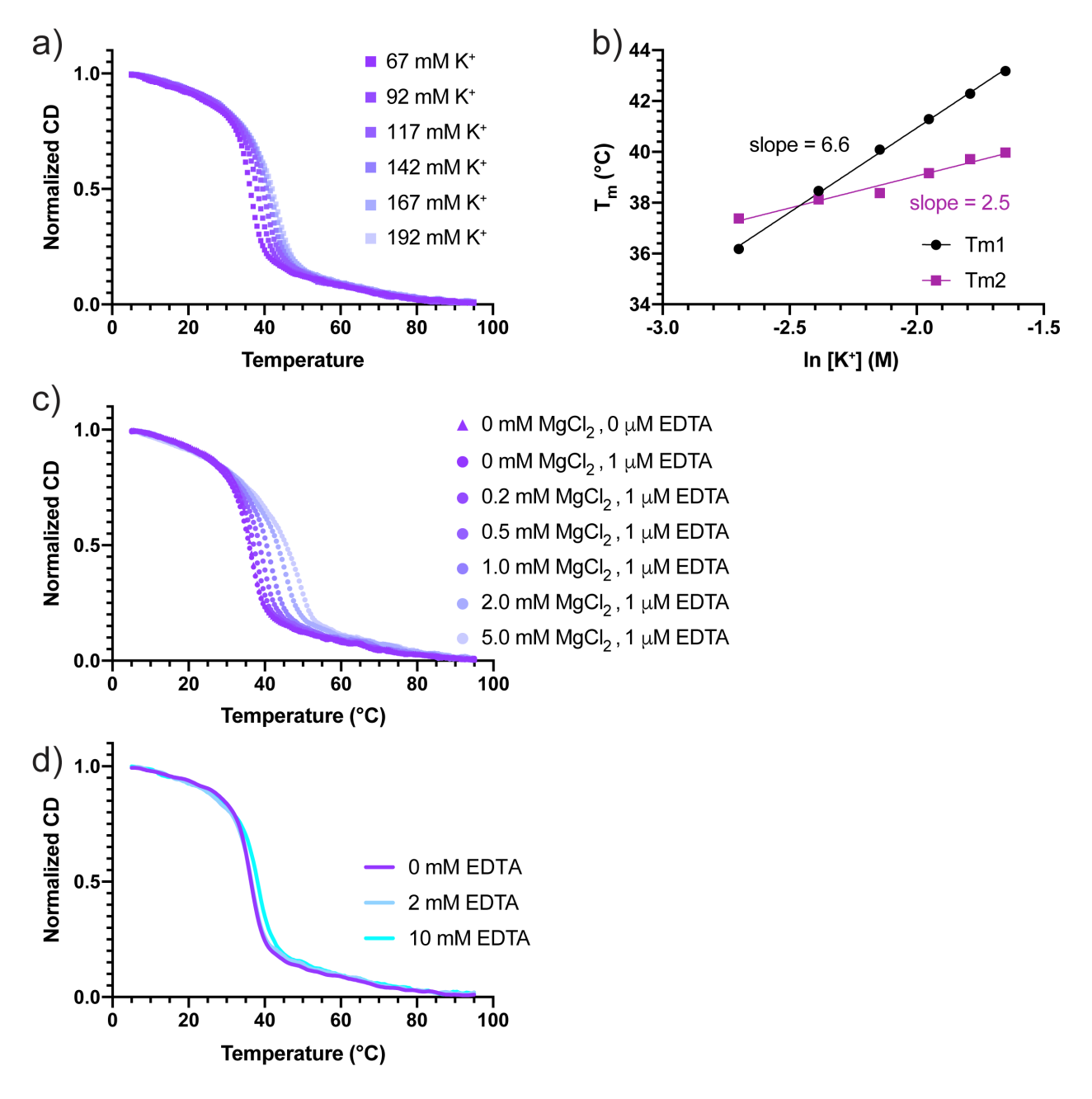


Figure S7. Thermal melting data of cssA under various ion conditions. (a) Thermal denaturation experiments of the cssA RNAT with increasing KCl. Figure legend indicates the total concentration of K^+ in the buffer. (b) Plot of T_m vs. $ln[K^+]$ to analyze the ion-dependence of unfolding. (c) Titration experiments of the cssA RNAT with increasing concentration of MgCl₂. Figure legend indicates the concentrations of MgCl₂, and EDTA added to the standard buffer. (d) Thermal denaturation of prfA RNAT in the presence of high concentrations of EDTA. All CD data were monitored at 260 nm and normalized between 0 and 1 for comparison.

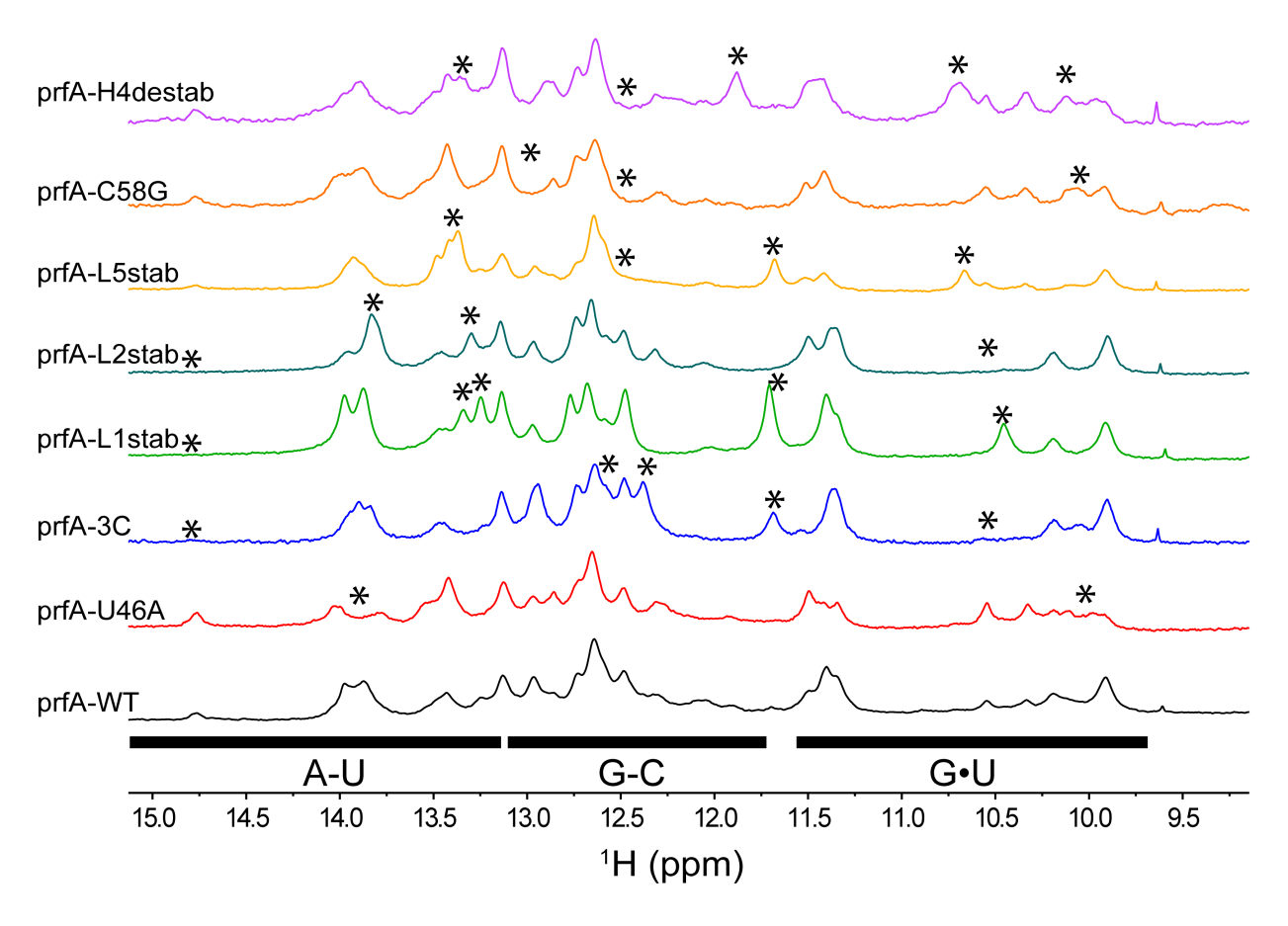


Figure S8. Overlay of imino proton spectra for prfA-WT and mutant RNATs. Qualitative analysis of imino proton spectra of prfA-WT and various mutant RNATs is consistent with local changes, as would be expected by the mutations introduced. Changes in individual spectra relative to WT are indicated by *. Imino proton spectra were collected at 20 °C.

Supplemental References:

- [1] Kaur, H., Arora, A., Wengel, J., and Maiti, S. (2006) Thermodynamic, counterion, and hydration effects for the incorporation of locked nucleic acid nucleotides into DNA duplexes, *Biochemistry* 45, 7347-7355.
- [2] Watts, J. K., Martin-Pintado, N., Gomez-Pinto, I., Schwartzentruber, J., Portella, G., Orozco, M., Gonzalez, C., and Damha, M. J. (2010) Differential stability of 2'F-ANA*RNA and ANA*RNA hybrid duplexes: roles of structure, pseudohydrogen bonding, hydration, ion uptake and flexibility, *Nucleic Acids Res* 38, 2498-2511.